

Contents lists available at ScienceDirect

## Mechanical Systems and Signal Processing

journal homepage: www.elsevier.com/locate/ymssp





# Experimental full waveform inversion for elastic material characterization with accurate transducer modeling

Md Aktharuzzaman<sup>a</sup>, Shoaib Anwar<sup>a</sup>, Dmitry Borisov<sup>b</sup>, Jiaze He<sup>a,\*</sup>

- a Department of Aerospace Engineering and Mechanics, The University of Alabama, Box 870280, Tuscaloosa, 35487, AL, USA
- <sup>b</sup> Kansas Geological Survey, The University of Kansas, KS, Lawrence, KS, USA

#### ARTICLE INFO

Communicated by L. Jankowski

Keywords: Material characterization Ultrasound computed tomography Full waveform inversion Transducer modeling Spectral element method

#### ABSTRACT

For quality assurance and in-service safety, sufficient characterization of the materials is essential during the development, manufacture, and processing of a material in any industrial setting. Evaluation of elastic coefficients, material microstructures, morphological features, and related mechanical properties are all part of the process of characterizing a material. Ultrasonic signals are sensitive to material properties such as wave speeds, attenuation, diffusion backscattering, microstructural variation, and elastic characteristics (e.g., elastic modulus, hardness, etc.). Ultrasonic computed tomography (USCT) is an emerging imaging method that can be implemented to obtain a quantitative estimation of material properties. In this study, a source estimation technique was initially proposed to obtain the source time function for accurate forward modeling by constructing a linear inverse problem for the unknown transducer modeling. Finally, a material characterization approach was proposed with accurate source estimation to extract wave speed distribution from an elastic material by employing a wavebased method, known as full waveform inversion (FWI). Systematic performance analysis of the proposed FWI model with accurate source estimation was assessed using experimental and synthetic data obtained from a 6061 aluminum sample. Overall, the proposed FWI technique has successfully reconstructed the wave speed distribution, exhibiting the potential of the proposed method of material characterization in various engineering applications.

## 1. Introduction

Understanding the characteristics of a material is very important to model and effectively design many products in any engineering application, especially in manufacturing industries. It is often challenging to achieve sufficient quantitative information about the material through traditional characterization techniques [1]. In recent times, metal Additive Manufacturing (AM) is increasingly being used to make functional components where one of the barriers for AM components to become mainstream is the difficulty to characterize them [2-4]. AM components can have widely different properties based on process parameters, Improving any AM process requires understanding process structure-property correlations, which can be gathered in situ and post-process through nondestructive and destructive methods. Defects in AM components are inherently geometry-dependent; hence, functional AM components must be certified on a case-by-case basis. Complex and varying AM procedures often impact the microstructure (e.g., grain size and phase), which tends to dictate mechanical properties like hardness, yield strength, ultimate tensile strength, elastic modulus, etc. [5].

https://doi.org/10.1016/j.ymssp.2024.111320

Corresponding author. E-mail address: jiazehe@gmail.com (J. He).

Ultrasound offers a wide variety of techniques for material characterization through nondestructive evaluation (NDE), which has been used to qualify various processing treatments such as precipitation hardening, case hardening, and rolling texture, and to assess the damage of metallic components due to various degradation mechanisms like fatigue, creep, corrosion, and embrittlement [6]. Ultrasonic signals have distinctive acoustic features, such as ultrasonic velocity and attenuation, related to the elastic modulus and density [7]. An ultrasonic examination is usually volumetric, and can provide information about bulk material properties. Ultrasonic parameters are significantly affected by changes in microstructural or mechanical material properties. Elastic modulus and the density inside the polycrystalline or bulk materials control the velocity and attenuation of the ultrasonic wave, which in turn are related to the microstructure through variations in the elastic modulus of the individual grains, the orientation of the grains and relative amounts of the phases present [8–10].

Among various ultrasound characterization methods, the ray-based synthetic aperture focusing technique (SAFT) and time of flight (ToF) are very commonly used [11–13]. For structures with less complexity, the ray-based method can accurately calculate direct arrival and the reflected phases [14,15]. However, ray-based techniques are often ineffective for complex structures with various impedance contrasts and insufficient sensitivity as the physics is considered to be simplified [16]. On the other hand, wave equation-based imaging techniques are more effective because they consider not only the travel time (as in the case of ray-based theory) but also the amplitude and waveforms inside a complex structure involving full acoustic or elastic wave equations [17].

Ultrasound computed tomography (USCT) is an emerging tomography-based ultrasound imaging technique that relies on the transmission and reflection of ultrasonic energy through the object of interest. Full waveform inversion (FWI) is a partial differential equation-constraint, nonlinear optimization technique widely used in geophysical imaging [18,19]. FWI is based on full wave-field modeling and inversion to extract material parameter distribution using wave equations [20]. The FWI method generates a velocity model by iteratively determining and minimizing a waveform residual, which is the difference between the measured data and the modeled output.

FWI has emerged as a powerful imaging technique with diverse applications spanning various disciplines, including geophysics [21,22], oil and gas exploration [23,24], environmental monitoring [25], astrophysics [26,27], and numerous medical imaging applications [28]. In recent years, applying FWI to ultrasound tomography-based imaging in non-destructive testing (NDT) has shown promising results. Nguyen et al. [29] presented the FWI results in the detection of bridge-deck delamination. Köhn et al. [30] demonstrated that FWI using elastic Rayleigh waves provides the S-wave velocity map of a weathered sandstone sample. Rao et al. [31,32,33] successfully implemented FWI to ultrasonic-guided waves-based NDT and verified their findings with experimental data. They performed this research by using a multi-scale inversion and a 2D acoustic approximation to solve the wave equations in the frequency domain while conducting a large number of experiments. He et al. [34] studied the numerical evaluation of the performance of FWI for inclusion inversion in various complex metallic components in a water-bathed environment and thereby demonstrated the potential of applying FWI to complex structures. Anwar et al. [35,36] investigated the application of FWI to enhance imaging accuracy for assessing inclusion and porosity, specifically within the context of additive manufacturing processes through numerical studies.

FWI evaluates its data misfit measurements in the time or frequency domain. In FWI, the high dimensional gradient of the misfit function is efficiently computed using the adjoint state method [37,38]. The gradient is evaluated by interacting the back-propagated data misfit with the forward-propagated source wavefield. A new updated model is generated from the previous reference model and the computed scaled gradient at each iteration. The iterations continue until the data misfit falls below predefined thresholds or when other convergence measures are met. Such a process requires accurate temporal source function information. Significantly incorrect source information may force the inversion towards a local minimum, severely compromising the inversion and leading to significant artifacts in the resultant velocity model [39,40]. As a result, transducer modeling is one of the key components to accurate FWI results.

Ultrasonic transducers, that convert ultrasonic electrical signals to mechanical movement, can be modeled using various techniques that consider the electromechanical coupling effect. Both the finite element method (FEM) [41,42] and finite difference time domain (FDTD) [43] methods are frequently used to model the wave propagation excited by ultrasound transducers in a variety of applications. However, the transfer function of the transducer elements to represent this effect for FEM and FDTD modeling is sometimes unknown. Multi-physics-based modeling software (e.g., COMSOL [44] and ANSYS [45]) can also be employed to model ultrasonic transducers. For example, piezoelectric transducers can be modeled using piezoelectric constitutive equations, that relate the material's mechanical strain, electric field, and charge density. Multiphysics modeling approaches require these properties (e.g., piezoelectric coefficients) for accurate modeling. However, some transducer information is sometimes proprietary and unavailable to the end users. Additionally, factors such as couplant thickness are not fully controllable or measurable, thereby hindering the accurate modeling of transducers even with a multiphysics solver.

Based on the above discussion regarding transducer modeling, it is evident that by taking transducer response into account to characterize the transducer beam profile, one can add an extra layer of complexity to FWI. Instead, many researchers explored a more straightforward approach where source signature can be estimated based on an inversion scheme. Pratt [46] introduced a source estimation technique based on a linear inversion to extract source signatures from seismic exploration. This approach is computationally efficient, requiring only one forward simulation per source to estimate the source time function. Sandhu et al. [47] adopted a similar ultrasound waveform tomography technique for breast imaging with a ring transducer array in the frequency domain based on the least square ( $L_2$ -norm) misfit function. Suzuki et al. [48] suggested a source estimation technique comparable to the abovementioned approach, effectively reducing the value of any cost function. However, the success of such a source estimation approach in NDE-based material characterization using FWI has not been explored yet. This study proposes a source estimation approach in elastic FWI for nondestructive material characterization and numerically and experimentally benchmarks

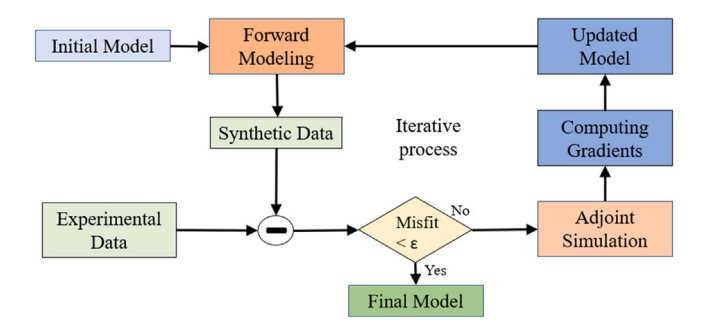


Fig. 1. Schematic diagram of Full Waveform Inversion (FWI) process.

the material reconstruction results. In our preliminary study [49], we demonstrated the feasibility of FWI for reconstructing wave speed distribution through numerical simulations. Additionally, we established the robust modeling capability of the spectral element solver and introduced the transducer modeling technique in support of our proposed methodology.

The elastic FWI using ultrasonic bulk waves was initially evaluated in an elastic medium for a range of frequencies and velocity distributions inside the domain corresponding to the variations in microstructural features. We then proposed a source estimation technique to obtain the source time function for accurate forward modeling by constructing a linear inverse problem for the unknown transducer modeling. The performance of the proposed FWI model with accurate source estimation was assessed using experimental and synthetic data obtained from a 6061 aluminum sample. This paper is organized as follows. In Section 2, the principles of FWI in elastic material characterization are introduced. In Section 3, micro-scale resolution investigations to demonstrate the potential of the proposed FWI method for elastic material characterization are presented while benchmarking the imaging performance of FWI. The experimental scanning setup is described in Section 4. The transducer source estimation workflow is described in Section 5. The validation of the estimated sources is also presented. The performance of FWI-based USCT in elastic material characterization with the estimated source utilizing both numerical data and experimental measurements is investigated in Section 6 and discussed in Section 7. Finally, conclusions are summarized in Section 8.

#### 2. Full waveform inversion theory for material characterization

As a way of introducing terminology used in the subsequent sections for inversion, the theory of full waveform inversion (FWI) was briefly reviewed. As shown in Fig. 1, the FWI process includes selecting sources and an initial model, conducting forward simulations, evaluating the data misfit, back-projecting the measured waveform difference, and optimizing the simulated model until the measured and simulated signals ideally converge on a single underlying model [34]. The goal is to create a final model that accurately represents actual model properties and minimizes the discrepancy between the experimental data and the signals collected at the same corresponding locations in the numerical simulations (synthetic data).

## 2.1. Forward modeling

We can represent the equation of motion for elastic materials in terms of a three-component displacement wavefield  $s(\mathbf{x},t)$  [50],

$$\rho \partial_t^2 \mathbf{s} = \nabla \cdot \mathbf{T} + \mathbf{f} \quad , \tag{1}$$

where  $\rho$  denotes mass density, **T** is the stress tensor, and **f** is the excitation forces. In this study, the excitation force **f** was considered as a point source. In an elastic medium,

$$T = C : \nabla s$$
 (2)

where C is the stiffness tensor representing the elastic characteristics of the media. Here, ":" refers to the double dot product. Note, for anisotropic material, it can hold the fully anisotropic tensor with 21 independent parameters [51]. Therefore, Eq. (1) can be written in terms of displacement field as

$$\rho \partial_t^2 \mathbf{s} = \nabla \cdot (\mathbf{C} : \nabla \mathbf{s}) + \mathbf{f} \quad . \tag{3}$$

#### 2.2. Adjoint simulation

The synthetic waveform data, described in Section 2.1, is compared with real waveform data to calculate misfit between the synthetic and experimental measurements. For seismic inversion, Tarantola [52] introduced the least-squares waveform misfit function. In this study, the misfit function was defined for a single source as

$$\chi(\mathbf{m}) = \frac{1}{2} \sum_{r=1}^{N} \int_{0}^{T} \|\mathbf{s}(\mathbf{x}_{r}, t; \mathbf{m}) - \mathbf{d}(\mathbf{x}_{r}, t)\|^{2} dt \quad , \tag{4}$$

where **m** is the model space in ultrasound tomography, which is the parameters defining the elastic properties of the material, and  $\mathbf{d}(\mathbf{x}_r,t)$  and  $\mathbf{s}(\mathbf{x}_r,t;\mathbf{m})$  are the experimental and synthetic signals, respectively at N receivers locations  $x_r$ ,  $r=1,\ldots,N$ . Both wavefield data are windowed on the time interval [0,T].

In this study, the density is assumed to be constant and the effects of attenuation in the inversion is neglected [53]. The goal of FWI is to minimize the misfit function iteratively in the descent direction. The gradient of the misfit function is

$$\delta \chi(\mathbf{m}) = \sum_{r=1}^{N} \int_{0}^{T} \left[ \mathbf{s}(\mathbf{x}_{r}, t; \mathbf{m}) - \mathbf{d}(\mathbf{x}_{r}, t) \right] \cdot \delta \mathbf{s}(\mathbf{x}_{r}, t; \mathbf{m}) dt \quad , \tag{5}$$

where  $\delta s(\mathbf{x}_r, t; \mathbf{m})$  is the perturbations in the displacement field  $s(\mathbf{x}_r, t; \mathbf{m})$  due to the model perturbations  $\delta \mathbf{m}$  [37,54]. By introducing "adjoint sources" into the equation of wave motion as source time functions at the location of receivers, the adjoint wavefield is computed to determine how to update the velocity model for misfit reduction [37]. The adjoint wavefield can express using adjoint state methods (details can be found in [37,55]) by,

$$\rho \partial_{\mathbf{r}}^{2} \mathbf{s}^{\dagger} = \nabla \cdot (\mathbf{C} : \nabla \mathbf{s}^{\dagger}) + \mathbf{f}^{\dagger} \quad , \tag{6}$$

where  $\mathbf{s}^{\dagger}$  and  $\mathbf{f}^{\dagger}$  are adjoint wavefield and adjoint sources, respectively. The adjoint sources for least-squares misfit function can be expressed as data residuals by,  $\mathbf{f}^{\dagger} = \sum_r [\mathbf{s}(\mathbf{x}_r, T-t) - \mathbf{d}(\mathbf{x}_r, T-t)] \delta(\mathbf{x}_r - \mathbf{x})$ .

With the calculated adjoint wavefield, the equation can be rewritten (5) using the sensitivity kernel [37,54],

$$\delta \chi(\mathbf{m}) = \int (\delta \rho K_{\rho} + \delta C :: \mathbf{K}_{c}) d^{3}x \quad , \tag{7}$$

where

$$K_{\rho}(\mathbf{x}) = -\int \mathbf{s}^{\dagger}(\mathbf{x}, T - t) \cdot \partial_t^2 \mathbf{s}(\mathbf{x}, t) dt \quad , \tag{8}$$

$$\mathbf{K}_{c}(\mathbf{x}) = -\int \nabla \mathbf{s}^{\dagger}(\mathbf{x}, T - t) \nabla \mathbf{s}(\mathbf{x}, t) dt \quad . \tag{9}$$

These sensitivity kernels from all sources are combined to form a gradient that defines how the model parameters should be updated. The typical method is to use a gradient- or Hessian-based algorithm to minimize the overall misfit function rather than treating FWI as resolving a linear system [38,56]. The gradient-based technique (e.g., steepest descent method [57]) updates the model by simply using the gradient but usually converges slowly [58]. In contrast, a Hessian-based approach (e.g., Newton's method, Gauss–Newton method) uses both the gradient and the Hessian (a second-order derivative of the misfit function) to provide a model update [59]. In the Hessian-based technique, the new model ( $\mathbf{m}_{new}$ ) can be defined from the previous model ( $\mathbf{m}_{old}$ ) by,

$$\mathbf{m}_{new} = \mathbf{m}_{old} + \alpha \mathbf{H}_{old}^{-1}(-\mathbf{g}_{old})$$
 (10)

where **g** is the first-order derivatives of  $\chi$ ( **m**), **H** is the Hessian matrix (a second-order derivative of the misfit function), and  $\alpha$  is the step length [60]. However, the cost of computing the inverse of Hessian for a nonlinear optimization problem in FWI is impermissibly high. Consequently, the Hessian-based technique suffers from expensive computing costs and massive storage requirements.

The Gauss-Newton method has been proposed to alleviate the high computing costs, where the misfit function is approximated as a sum of squares of linear functions. The Hessian matrix (second-order derivative), **H**, of the misfit function, is approximated by the Jacobian matrix (first-order derivative) of the linear functions [61]. This approximation results in a simplified quadratic model of the misfit function that can be minimized analytically. The matrix-vector product of the inverse of the estimated Hessian and the gradient at each iteration is required in the Gauss-Newton method to determine the descent direction, which is computationally intensive for large-scale datasets. On the contrary, the quasi-Newton method, such as Broyden-Fletcher-Goldfarb-Shanno (BFGS) [60], Limited-memory Broyden-Fletcher-Goldfarb-Shanno (L-BFGS) [62], outperforms the Gauss-Newton method for the large-scale optimization problem, especially in FWI [63]. In this study, the L-BFGS optimization algorithm is implemented to update the model.

## 3. Benchmarking imaging performance

Ultrasonic wave speeds in elastic material, especially AM metals, are sensitive to microstructures [64,65]. The polycrystalline distribution of the grains in AM metals is inherently anisotropic. He et al. [53], in their recent work, presented the inversion for anisotropic materials for a 2D numerical model. However, in this study, the aim is to benchmark the imaging performance of FWI when the material property distribution can be treated as isotropic. Micro-scale resolution studies are also include to illustrate the potential of the proposed method for material characterization. Moreau et al. [66] introduced a laser ultrasonic (LUS) system for in-situ non-contact measurements of the mechanical properties, e.g., elastic moduli, microstructural phase transformation with temperature, some measure of crystallographic texture, and grain growth of metals. Mutlu et al. [10] in their study presented that the ultrasonic measurements (e.g., longitudinal wave speed) in AISI H13 tool steel alloy correlate to the microstructural phase permitting nondestructive characterization of microstructure in steels.

Rivera et al. [67] discussed the microstructures and mechanical behavior of Inconel 625 fabricated by solid-state additive manufacturing (SSAM). The microstructure of the as-built Inconel 625, which consisted of a distribution of grains in various

Table 1
Wave speeds of the models.

Models		$V_p$ (m/s)	$V_s$ (m/s)
Initial model		5920.5	3180.08
True model	Top layer	6077–6091 average: 6075	3294–3322 average: 3308
	Middle layer	5821–5838 average: 5832	3213–3239 average: 3224
	Bottom layer	5750–5795 average: 5773	3049-3088 average: 3068
	Outer region (light green)	5920.5	3180.08

shapes and sizes at different layers, was presented in this study. A numerical model was established, taking inspiration from the abovementioned study to benchmark the imaging performance and evaluate the feasibility of the proposed FWI algorithm. The numerical model was developed and solved by a 2D spectral element-based solver (SPECFEM2D [50]). A python basedworkflow (Seisflows [68]) was modified to implement FWI. Three velocity regions in this numerical model represent three layers of microstructures with distinct velocity distributions inside each layer as shown in Fig. 2(c) and (d), which was considered as the true model. The domain size was 1 mm by 1 mm. For the entire paper, unless explained otherwise, the center of the domain is assumed to be the origin of the reference coordinate system. The true model was constructed with three layers of different velocity ranges in the middle of the domain (-0.375 mm to 0.375 mm). For different microstructural patterns, bulk wave speeds inside the materials should be random [67]. Therefore, in each layer, there were small square regions with slightly different velocities, each aiming to represent a grain approximately from the sizing (other than anisotropy) perspective. The upper-velocity distribution layer (in Fig. 2(c) and (d)) had a higher velocity range (average  $V_p$ : 6075 m/s and  $V_s$ : 3308 m/s) compared to the bottom two layers (middle layer with average  $V_p$  was 5832 m/s and  $V_s$  was 3224 m/s and bottom layer with average  $V_p$  was 5773 m/s and  $V_s$  was 3068 m/s). The outside of this middle domain (red region in Fig. 2(c) and (d)) had a constant  $V_n$  and  $V_s$  of 5920.5 m/s and 3180.08 m/s, respectively. The initial model was composed of homogeneous background models with constant  $V_n$  and  $V_s$  wave speeds of 5920.5 m/s and 3180.08 m/s throughout the entire domain (Fig. 2(a) and (b)). For simplicity, a constant density of 7830 kg/m<sup>3</sup> was considered for both initial and true models in this study. The material properties of the model are shown in Table 1.

To scan this specimen, four evenly spaced linear arrays were distributed in the range of -0.5 mm to 0.5 mm at four boundaries to fully surround the region. Each linear array contains 16 elements, and all elements of each array were excited individually. Thus, 64 such excitation events were generated that partially simulate possible non-contact laser-based scanning systems (e.g., [69,70]) to form a synthetic aperture data acquisition setup on the surface of the materials. All four surrounding linear arrays (a total of 124 equally spaced receiver elements) were used to collect the displacement signals (both in horizontal and vertical velocity components). The excitation signal used in this section is a Ricker signal.

To benchmark and analyze FWI's material characterization performance for both texture types and at grain levels, two center frequencies, 8 MHz and 25 MHz, were considered, respectively. Implementing FWI for complex structures with high frequency can cause a cycle-skipping phenomenon, where the misfit function converges to a local minimum due to lack of accuracy in the initial model [18]. Therefore, an incremental frequency ramp-up strategy was adopted, transitioning from 8 MHz to 25 MHz through a systematic progression of 1 MHz at each subsequent ramping stage (with 100 iterations), rather than directly applying the 25 MHz frequency to the initial model. A detailed description of such an approach for highly nonlinear, anisotropic inversions can be found in [53]. To reduce artifacts caused by the boundary wall reflection and scattered waves in the outer region (the light green region in Fig. 2(c), (d)), a mask was used so that this region would update in the simulation. In Fig. 3, elastic wavefield snapshots when the excitation source is at (0.03 mm, 0.5 mm) are shown, at  $0.00075 \mu s$ ,  $0.075 \mu s$ ,  $0.15 \mu s$ , and  $0.225 \mu s$ .

For an 8 MHz center frequency, Fig. 2(e) and (f) exhibit the reconstruction of  $V_p$  and  $V_s$  at the 100th iteration. While the velocity differences among the three layers were detected for both  $V_p$  and  $V_s$ , the velocity distribution at each layer was not clearly observed. The reconstruction results for a 25 MHz center frequency at 98th iteration for both  $V_p$  and  $V_s$  are shown in Fig. 2(g) and (h). The velocity differences across the layers along with the velocity distribution within each layer were detected convincingly for 25 MHz. It is notable from Fig. 4(a) and (b) that data misfits were reduced for both 8 MHz and 25 MHz.

In addition, to have better insights regarding the reconstruction of the overall velocity distributions, an arbitrarily chosen line at x=0.0066 mm across the z-axis was considered, and velocities (for both  $V_p$  and  $V_s$ ) across this line are plotted in Fig. 2(i) and (j). The overall velocity distributions throughout the z-axis were better reflected by the line at x=0.0066 mm. In Fig. 2(i) and (j), green and yellow dashed lines represent the velocities of the true model and initial model, respectively and the blue and red solid lines represent the inverted velocities from the proposed FWI model at 25 MHz and 8 MHz, respectively. The variations in inverted velocities, both  $V_p$  and  $V_s$ , in various domain regions for both 8 MHz and 25 MHz frequencies were broadly consistent with the true models. The difference in velocity distributions between the inverted model and the true model is smaller for 25 MHz than that for 8 MHz. Hence, reconstructed images looked sharper at 25 MHz. As  $V_s$  was almost half of the  $V_p$ , the wavelength with  $V_s$  was likewise around half of the wavelength with  $V_p$ , which allowed for better reconstruction of  $V_s$  map than the  $V_p$  map. Comparing the reconstructed results from Fig. 2(e)–(j), it is clear that contrary to the 8 MHz model, the 25 MHz model provides a better reconstruction of the velocity distributions across the layer as well as inside each layer.

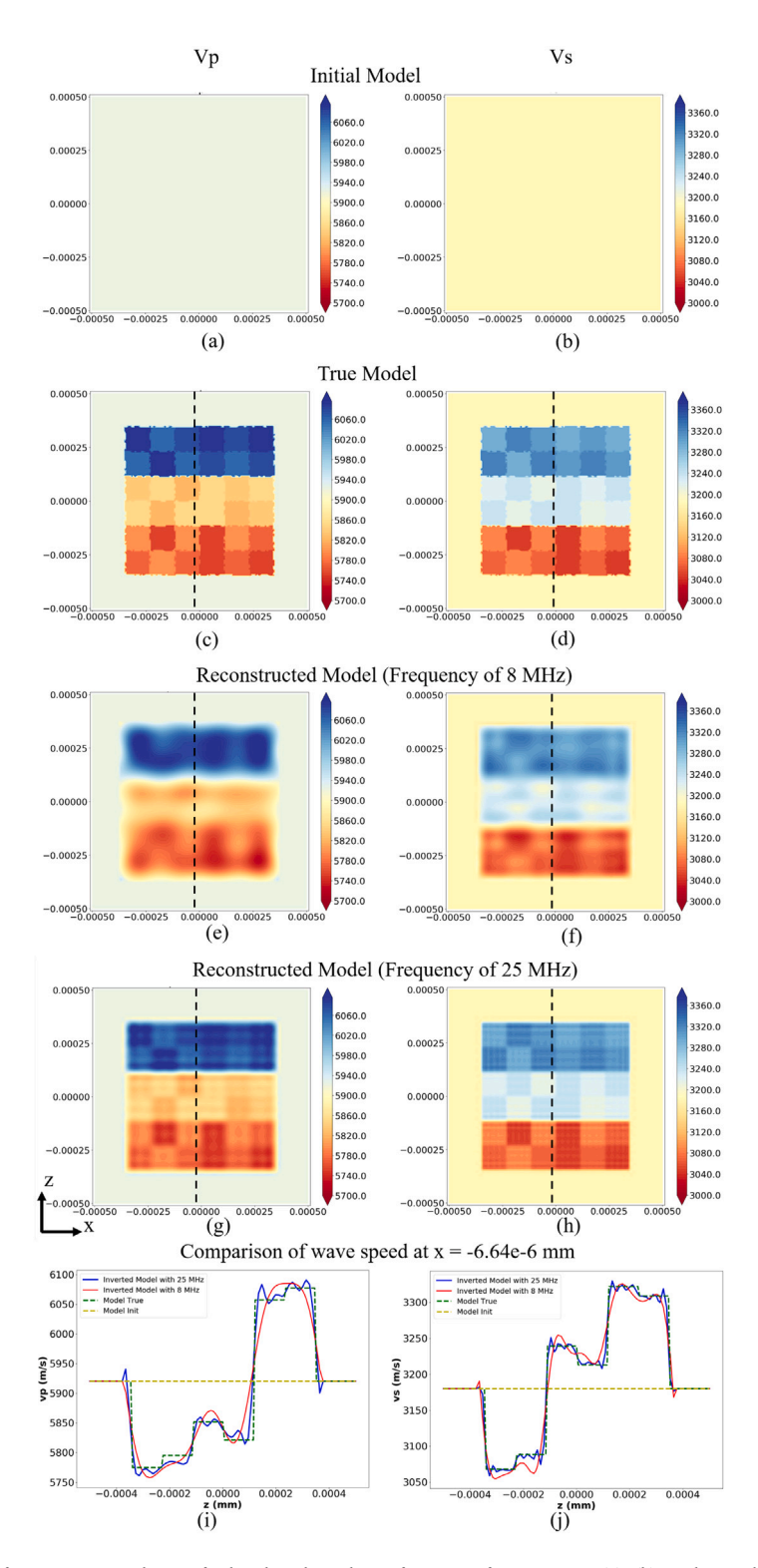


Fig. 2. Computational model of 1 mm  $\times$  1 mm domain for benchmarking the performance of FWI. Figures (a), (b) are longitudinal wave speed ( $V_p$ ) and shear wave speed ( $V_s$ ) of the initial model, (c), (d) are  $V_p$  and  $V_s$  of the model true, (e), (f) are  $V_p$  and  $V_s$  of inverted images of the model with 8 MHz frequency at the 100 th iteration, (g), (h) are  $V_p$  and  $V_s$  of inverted images of the model with 25 MHz frequency at the 98 th iteration and (i), (f) is  $V_p$  and  $V_s$  comparison of inversion models with 8 MHz and 25 MHz at x = -6.641275e - 06 mm, respectively.

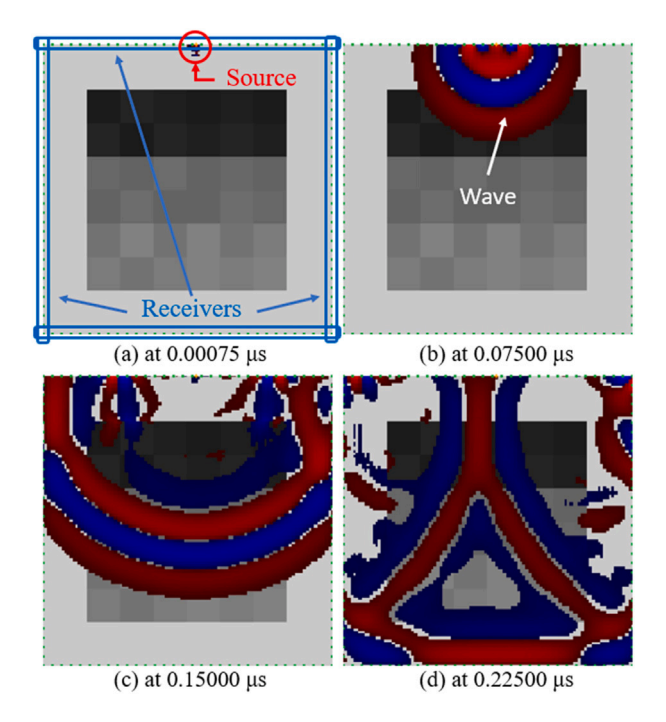


Fig. 3. Wave propagation simulations using the source at (0.03 mm, 0.5 mm) with 25 MHz center frequency at the time (a)  $0.00075 \, \mu s$ , (b)  $0.075 \, \mu s$ , (c)  $0.15 \, \mu s$  and (d)  $0.225 \, \mu s$ . (For all the simulations in this paper, the center of the domain is assumed to be the origin of the reference coordinate system.)

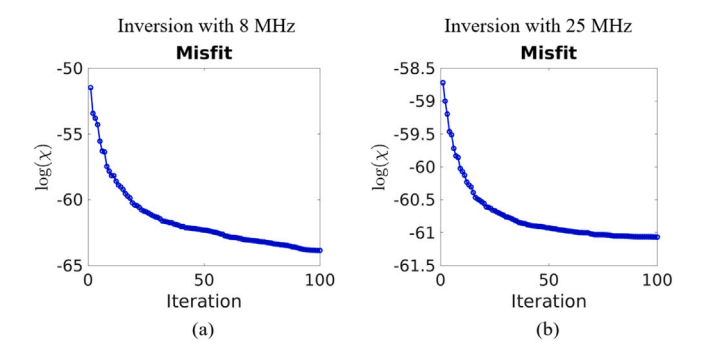


Fig. 4. Misfit function over iterations (in log scale) for (a) Inversion with 8 MHz frequency and (b) Inversion with 25 MHz frequency.

## 4. Experiments

#### 4.1. Experimental scanning setup

An experiment using two linear transducer arrays as both sources and receivers was conducted to evaluate the approaches proposed for ultrasound tomographic imaging of an elastic specimen. A multi-channel data acquisition (DAQ) system from Verasonics (Fig. 5(c)) was used to acquire data from every possible source-receiver combination. Experimental measurements were performed on a 300 mm by 101 mm by 51 mm 6061-aluminum block shown in Fig. 5(a) and (b). Two linear transducer arrays with a center frequency of 0.5 MHz, each containing 32 identical transducer elements, were used in this experiment. The array elements spacing (i.e., pitch) for each transducer was 2 mm. This experiment was performed at a relatively low center frequency of 0.5 MHz because lower ultrasonic frequency results in less attenuation, allowing for deeper penetration depth and a wider coverage range [71]. Glycerin (Couplant B2 from Olympus) was used as couplant in this study. There are high acoustic impedance mismatches between air and the test specimen. Glycerin can transmit sound energy more effectively by reducing the acoustic impedance mismatch.

#### 4.2. Synthetic model

To perform the FWI using experimental measurements from the scanning setup mentioned in Section 4.1, a corresponding array setup in SPECFEM2D (see Fig. 6) was used for generating scanning data. The source elements were assumed to be point sources.

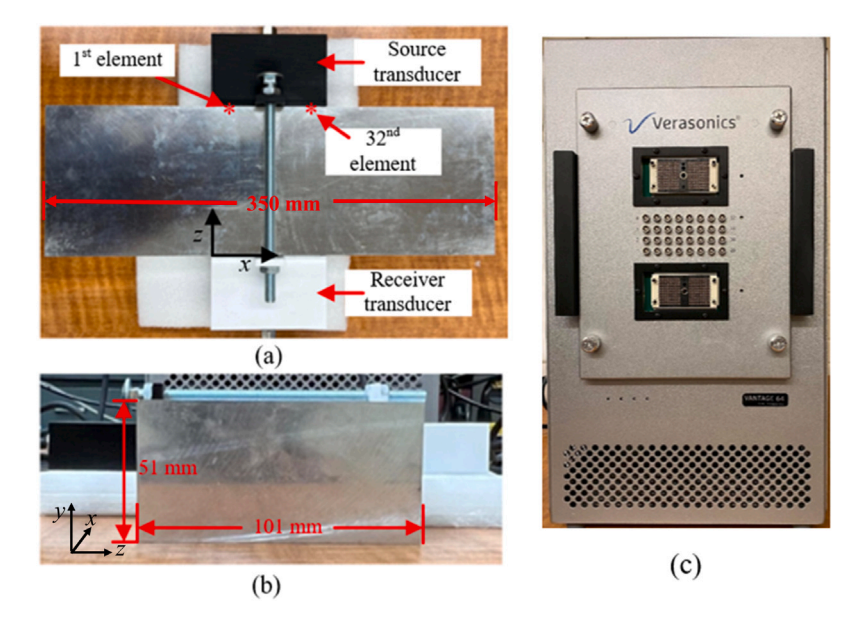


Fig. 5. Ultrasonic scanning setup for aluminum specimen using two 32-elements linear phased array transducer in transmission mode. (a) top view (b) side view (c) multi-channel Verasonics data acquisition system.

The specimen used in the experiment had a considerably large horizontal dimension, making it easy to exclude the reflected signals from the specimen's left and right boundaries. Therefore, only a 101 mm by 101 mm domain (depicted in Fig. 6) was modeled to reduce computational costs. The synthetic model's left and right boundaries are subjected to absorbing boundary conditions. Receiver array elements were placed at the bottom surface of the domain (marked in green). The spacing (i.e., pitch) between two adjacent receiver elements was 2 mm, and the number of receiver elements was 32. Each source element was placed at the top of the domain. In this study, the array elements of the source and receivers were numbered from left to right. For example, the Source 4 location is marked as a yellow cross in Fig. 6, which is 24.5 mm away from the left boundary. To perform the inversion for unknown materials, we purposefully assumed the initial model with an incorrect  $V_p$  of 6410 m/s.  $V_s$  was calculated based on the assumed  $V_p$  to create the initial background model. Additionally, a constant density of 2660 kg/m³ was assumed. This model was used in the following sections in the transducer source estimate framework and as an initial model in the FWI.

## 5. Transducer source estimation framework

## 5.1. Source estimation workflow

This section describes the general workflow of the proposed source estimation process. The synthetic model discussed in Section 4.2 is utilized where, to represent a calibration block, the assumption was that the source was the only unknown term and the velocity distribution was correct. To keep the synthetic and the experimental measurements in a consistent scale, normalized signals throughout the source estimation process were considered. The workflow of the proposed source estimation process is shown in Fig. 7.

First, experimentally acquired signals must be windowed in order to receive only the longitudinal waves (P-waves). Then, the noise from the experimental measurements was filtered out. The measured data were then muted to remove all energy beyond the direct arrival. The main goal is to mute any energy arriving beyond P-waves because FWI in this work will only fit P-waves. The time windowing of the direct arrivals from experimental measurements is a very crucial step in the source estimation process and ensures the elimination or at least suppression of the shear wave (SV-wave) effects from the experimental measurements.

A synthetic model based on the scanning setup (described in Section 4.2) is required to generate synthetic data. later in this process, the synthetic data, will be compared with the experimental measurements to extract the source signal. Different signals (e.g., Ricker, Gaussian, tone burst) can be considered as source time functions in the initial model. This selected unknown signal should have a wider frequency bandwidth compared to that of the experimental source transducer (i.e., 0.5 MHz). A wider frequency range is necessary to ensure that the process accounts for all of the useful frequencies of the actual source signals. As a result, the first derivative of the Gaussian function was selected as the initial synthetic source time function.

The synthetic and the experimental measurements in the same time frame were converted in the frequency domain by performing Fast Fourier Transform (FFT). A complex-valued scaling factor can be introduced to represent the mechanical source in the model with respect to a known source. Correspondingly, the source signature can be estimated by optimizing a complex-valued scaling factor utilizing the synthetic and experimental measurements in the frequency domain. The detailed formulation is described in Section 5.2. An inverse Fourier transform was performed to achieve the estimated source function in the time domain.

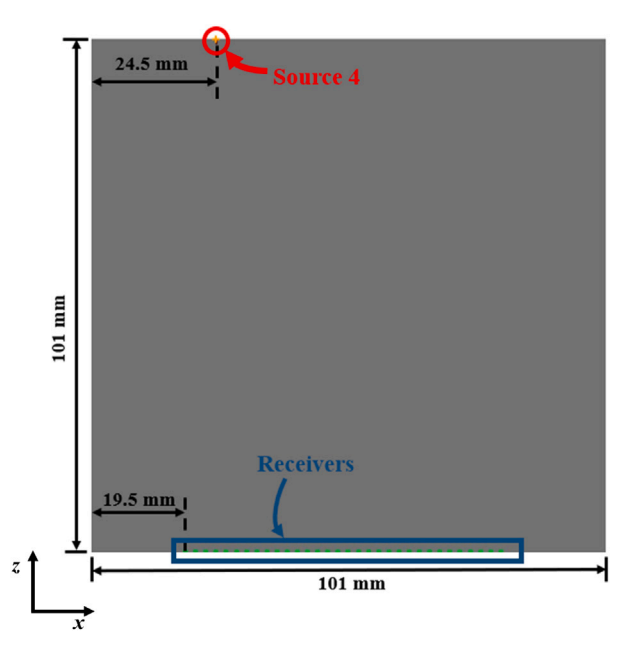


Fig. 6. Dimension of the synthetic model based on the experimental setup showed in Fig. 5. Source 4 position is marked which is 24.5 mm from the left boundary. 32 receivers elements (green lines) are placed at the bottom surface.

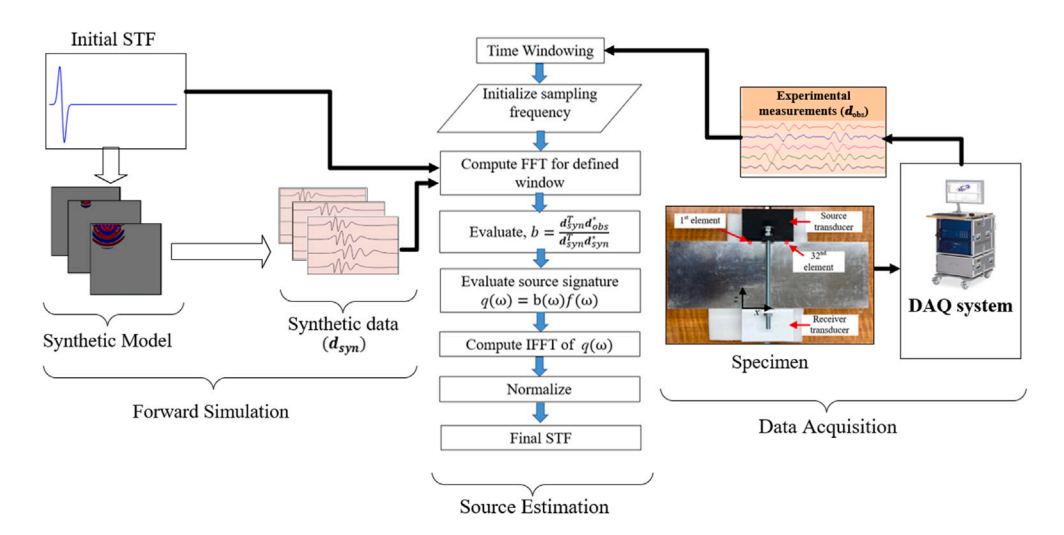


Fig. 7. The flow chart of the proposed source estimation process. Initial STF of the synthetic model, synthetic data, and experimental data are the input to the estimation process.

#### 5.2. Formulation of source estimation as a linear inverse problem

A synthetic model is considered with a known source signal that is arbitrarily selected with a wider frequency bandwidth compare to the experimental source transducer (i.e., 0.5 MHz). However, the source term required by the employed synthetic model is the mechanical source that is unknown. The ultrasound tomography acquisition setup, which is depicted in Fig. 5, is employed in this section to formulate the proposed source estimation process.

Although each element of the linear transducer array used in the scanning setup is rectangular in shape, a point source is assumed to be positioned in the middle of the rectangular-shaped element,  $x_s$ , in this formulation for 2D imaging model. Consequently, the scattering effect from out-of-plane structures is neglected [47,72]. The goal of this framework is to invert for a source time function (i.e., Q(t)) to serve as the mechanical input under this point source assumption to best represent the excitation force induced by an element in 2D simulation. After FFT, the resulting STF should have a series of frequencies ( $\omega_k$ , k = 1, 2, ..., K) within the bandwidth of the transducer. Equivalently, the goal is to invert for the STF at each of the selected frequencies (i.e.,  $q(\omega)$ ). For a specific frequency,  $\omega_k$ , the wavefield is measured by  $N_r$  and all receivers positioned at  $x_r$  locations can be expressed as  $\mathbf{d}_{obs}(\omega_k)$ .

For this source inversion,  $N_r$  receivers are employed. For a single frequency,  $\omega_k$ , the complex valued experimental measurements,  $\mathbf{d_{obs}}(\boldsymbol{\omega_k})$ , is a  $N_r \times 1$  column vector. The unknown source time function,  $q(\omega_k)$ , is a scalar term as one point source is considered in the formulation at  $\omega_k$ . The forward wave equation in the frequency domain can then be defined in compact form as,

$$\mathbf{d}_{\mathbf{obs}}(\boldsymbol{\omega_k}) = \mathbf{G}(x_r, x_s; \boldsymbol{\omega_k}) q(\boldsymbol{\omega_k}) \quad . \tag{11}$$

where  $G(x_r, x_s; \omega_k)$  ( $N_r \times 1$ ) is the Green's function at  $\omega_k$ , which depends on the source/receiver locations and the medium properties [73]. To implicitly create and obtain this  $G(x_r, x_s; \omega_k)$  matrix, the following synthetic simulation can be performed. The unknown  $q(\omega_k)$ , can be assumed to be linearly correlated with any known source time function,  $f(\omega_k)$ , with a unknown complex-valued scalar,  $b(\omega_k)$ .

Then the unknown STF at  $\omega_{\nu}$  can be represented as,

$$q(\omega_k) = b(\omega_k) f(\omega_k) \quad . \tag{12}$$

The explicit dependence of each term in Eq. (11) on  $\omega_k$ ,  $x_r$ , and  $x_s$  will be dropped henceforth for the sake of brevity. Eq. (11) can then be rewritten as,

$$\mathbf{d}_{\text{obs}} = \mathbf{G}bf \quad . \tag{13}$$

At this stage, a synthetic model (e.g., the one introduced in Section 4.2) can be built with the known source term f as,

$$\mathbf{d}_{\text{cvn}} = \mathbf{G}f \quad . \tag{14}$$

where  $\mathbf{d}_{\text{syn}}$  is the Fourier-transformed, complex-valued measured from the synthetic model which is arranged as an  $N_r$  column vector. The vertical component of the displacement is only considered in this source estimation process.

The only unknown term in Eq. (13) is the complex-value scalar, b, which needs to be computed at each specific frequency. It is notable that, Eq. (13) is linear with respect to the source term, f. From the above definition of the forward model incorporating the known source, f, and the unknown scalar term, b, a misfit function can be formulated by minimizing the sum of squared residual errors (the  $L_2$  norm misfit function) [74],

$$E = \frac{1}{2}\delta \mathbf{d}^T \delta \mathbf{d}^* \quad . \tag{15}$$

where  $\delta \mathbf{d}$  is the residual data mismatch. Based on the above formulation, the residual data mismatch,  $\delta \mathbf{d}$ , can also be expressed as  $\delta \mathbf{d} = b \mathbf{d}_{syn} - \mathbf{d}_{obs}$ . The superscript T represents the ordinary matrix transpose and the superscript \* represents the complex conjugate. As a result, the misfit function can be written as,

$$E = \frac{1}{2} [b\mathbf{d}_{syn} - \mathbf{d}_{obs}]^T [b\mathbf{d}_{syn} - \mathbf{d}_{obs}]^*$$

$$= \frac{1}{2} [b^2 \mathbf{d}_{syn}^T \mathbf{d}_{syn}^* - b\mathbf{d}_{obs}^T \mathbf{d}_{syn}^* - b\mathbf{d}_{obs}^T \mathbf{d}_{obs}^* + \mathbf{d}_{obs}^T \mathbf{d}_{obs}^*]$$

$$= \frac{1}{2} [b^2 \mathbf{d}_{syn}^T \mathbf{d}_{syn}^* - 2b\mathbf{d}_{syn}^T \mathbf{d}_{obs}^* + \mathbf{d}_{obs}^T \mathbf{d}_{obs}^*]$$

$$= \frac{1}{2} [b^2 \mathbf{d}_{syn}^T \mathbf{d}_{syn}^* - 2b\mathbf{d}_{syn}^T \mathbf{d}_{obs}^* + \mathbf{d}_{obs}^T \mathbf{d}_{obs}^*]$$
(16)

By minimizing the misfit function (Eq. (16)) with respect to the complex-value scalar term b, an exact solution can be obtained. Minimum misfit can be achieved when,

$$\nabla_b E = \frac{\partial E}{\partial b} = \frac{1}{2} [2b\mathbf{d}_{\mathbf{syn}}^{\mathbf{T}} \mathbf{d}_{\mathbf{syn}}^* - 2\mathbf{d}_{\mathbf{syn}}^{\mathbf{T}} \mathbf{d}_{\mathbf{obs}}^*] = 0 \quad . \tag{17}$$

Finally, the optimal complex valued source scaling factor, b, is achieved such that the synthetic and experimental measurements best match in a mean squared sense. The optimal scalar value, b, can be derived from Eq. (17) as,

$$b = \frac{\mathbf{d}_{\text{syn}}^{\text{T}} \mathbf{d}_{\text{obs}}^*}{\mathbf{d}_{\text{syn}}^{\text{T}} \mathbf{d}_{\text{syn}}^*} \quad . \tag{18}$$

The complex-valued scaling factor, b, can be multiplied with the initially assumed known source term, f, to get an estimation of an individual source signal of the experimental measurement. The magnitude spectrum of both synthetic and experimental measurements was normalized. In other words, in the inversion process, the phase of the frequency components was only matched neglecting the amplitude information, which may lead to residual artifacts. For each source, the forward model needs to be computed once to estimate the source wavelet, which is independent of the initial model [46]. Finally, an inverse Fourier transform can be performed to get the estimated source signals in the desired time domain.

## 6. Experimental results of source estimation and FWI

#### 6.1. Source estimation

In this section, the accuracy of the estimated source time function was investigated in a systematic approach. The inverted STFs were used to excite ultrasonic waves in the synthetic model of a SPECFEM simulation. The resulting received signals were compared with the experimental measurements, and the degree of matching was used to evaluate the accuracy of the estimated STFs. Only the P-waves were considered for source estimation and comparison of the signals. After explaining the selection of the known STF for the source estimation, the source inversion results using a single pair of source/receiver signals is introduced first. Then, the performance evaluation of the estimated STFs using the signals from multiple receivers for source inversion is summarized.

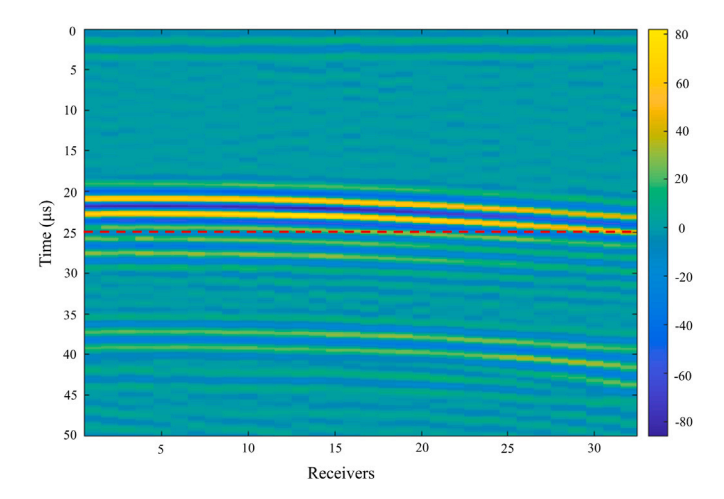


Fig. 8. Time space signals of experimental measurements when Source 4 was excited. The longitudinal waves reached Receiver 4 at about 25  $\mu s$  (marked by red dashed lines).

#### 6.1.1. Known source time function selection for source inversion

To demonstrate the source estimation process, the STF of the 4th element in the transmitting array (i.e., Source 4) was first inverted as an example. Then, in Section 6.1.4 the contribution of multiple receivers' to the source inversion process will be investigated. The source inversion in this section was performed by incorporating the A-scans.

The P waves from the experimental A-scan were first extracted by performing time windowing. P waves will reach receiver locations earlier than the shear wave since the P-waves travel faster than the shear waves. By closely observing the time-space signals for Source 4 (see Fig. 8), it is clear that most of the P-waves have been acquired by Receiver 4 at about 25  $\mu$ s. Therefore, the experimental signals were extracted up to 25  $\mu$ s to acquire only the P-waves. The time-windowed experimental A-scan at Receiver 4 is displayed in Fig. 9(c).

As described in the last section, the known STF for the synthetic model must have a wider frequency coverage than the source input induced by the transducer. The first derivative of the Gaussian function was selected as the known STF (see Fig. 9(a)). With the simulation domain described in Fig. 6, the corresponding received signal (Receiver 4 signal) using this known STF is shown in Fig. 9(b). The frequency spectrum of the received signals from both the simulation and the experiment (shown in Fig. 9(e)) shows that the bandwidth for the initial synthetic signal is wider than that of the experimental signal, indicating the suitability of the selected known STF.

In the proposed source inversion, the complex-valued unknown scalar term was computed in the frequency domain as explained in Section 5.2. Therefore, FFT was performed to convert the time domain signals from both experiment and simulation into the frequency domain. The data were discretized into 1750 frequency components with a sampling frequency of 0.041 MHz. Following the formulation described in Section 5.2, the unknown scalar factor (i.e., b) was computed at each frequency utilizing the normalized synthetic and experimental signals at Receiver 4. At each frequency, the computed scalar factor (i.e., b) was then multiplied to the known source term to calculate the actual source term (i.e., q) as shown in Eq. (12) in the frequency domain. Finally, inverse FFT was performed to obtain the inverted time-domain STF of Source 4 (see Fig. 9(d)). Forward simulation for Source 4 using this inverted STF was simulated to evaluate the quality of the estimated STF in the following subsection.

#### 6.1.2. Forward modeling accuracy for different receivers from the same source

To validate the accuracy of the estimated STF using a single A-scan signal and the experimental signals, the degree of matching between the simulated signals excited from the estimated STF at the same source location was investigated. Source-4 of the synthetic model was excited by the inverted STF using the Receiver-4 (i.e., A-scan to Source 4) as described in Section 6.1.1.

The comparison of the synthetic and experimental signals at Receiver 4 and Receiver 16 (both using the same inverted STF from Source 4's A-scan measurement) are highlighted in Fig. 10(a)–(b), respectively. It is evident from Fig. 10(a) that the synthetic A-scan signal at Receiver 4 is very well aligned with the experimental signal. However, there is a slight mismatch between the synthetic and experimental signal at the Receiver 16 location when Source 4 was excited, particularly in the latter portion of the signal (see Fig. 10(b)). Such mismatches of the signals at different receiver locations are expected due to the combination of the electromechanical effects and difference in incident angles.

## 6.1.3. Forwarding modeling accuracy when using STF inverted from different source-receiver measurements

In this section, the estimated STF was reconstructed at one source location and it were then used for excitation at a different source location in the forward simulation. The simulated signals was compared with the experimental measurement to evaluate the accuracy. The STFs of two source elements (Source 1 and 16) were separately inverted for this comparison. As shown in Fig. 5,

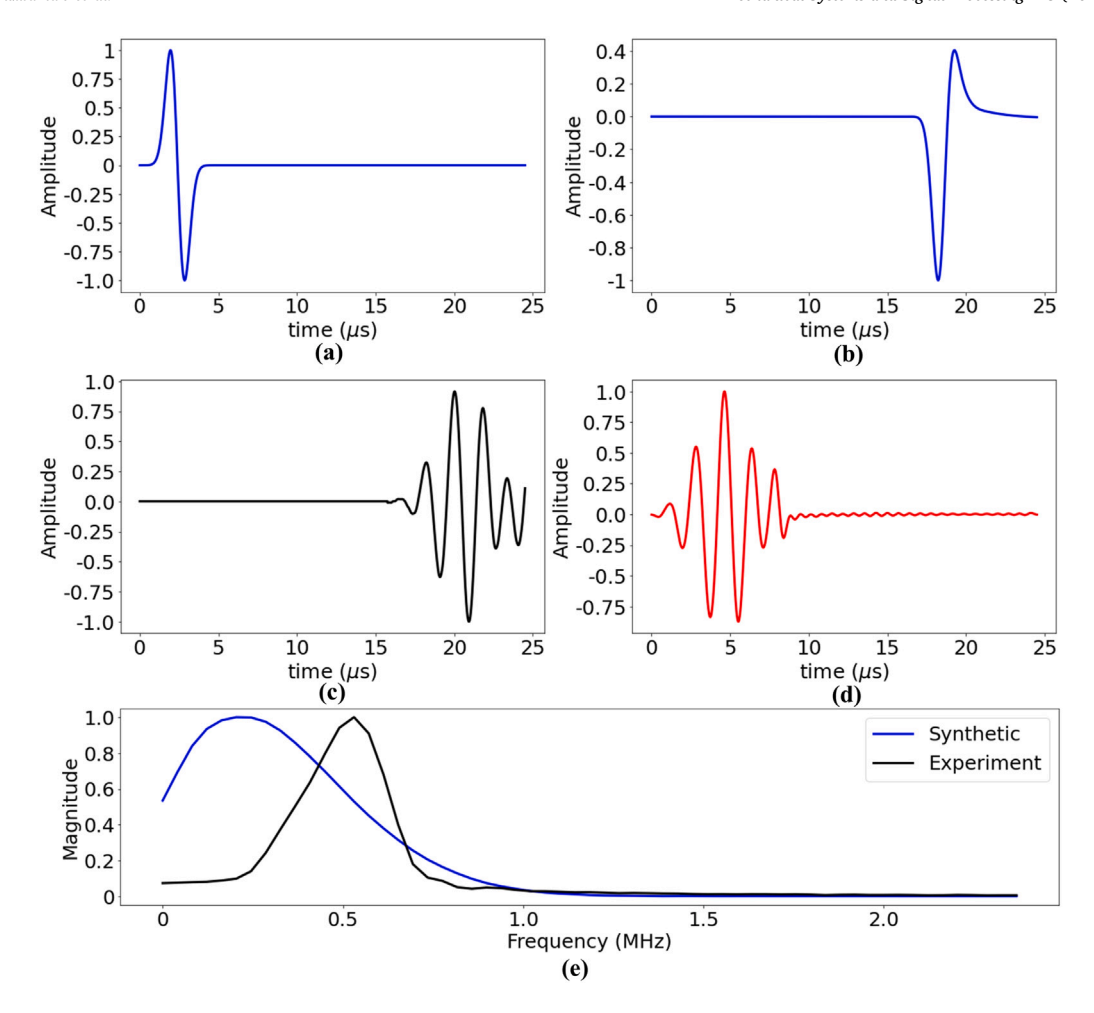


Fig. 9. (a) First derivative of Gaussian function as initial synthetic STF. (b) The signal at Receiver 4 location when Source 4 in the synthetic model was excited by the first derivative of the Gaussian function. (c) The experimental signal at Receiver 4 location when Source 4 is excited (i.e., A-scan). (d) Inverted STF of Source 4 using the signal at Receiver 4 location from synthetic and experimental measurements. (e) The frequency spectrum of both the initial synthetic signal and experimental signal at Receiver 4 location when Source 4 is excited.

Source 1 was located on the left side of the top array, while Source 16 was in the middle of the transducer array. The corresponding A-scan signals from Receivers 1 and 16 were separately used to invert the STFs for Source 1 and 16, respectively.

The effect of using an inverted STF from a different source was evaluated for the forward modeling at two source locations (Source 1 and Source 16). For each source location, two forward simulations were performed using (a) the STF inverted from its own A-scan and (b) the STF inverted from the A-scan of the other source. Comparisons were made for all signals received from the 32 receiving elements on the opposite side of the domain. To quantify the mismatch between each pair of the simulated and experimental signals,  $L_2$  norm was used to evaluate the misfit at each of the 32 receivers, as shown in Fig. 11. For Source 1 evaluation, Fig. 11(a) shows the 32 receiver misfits resulted from the two STFs — the green dots from the STF inverted using the A-scan of Source 1 (i.e., its own A-scan) and the red crosses from the STF inverted using the A-scan of Source 16 (i.e., a different source). The misfit values are consistently lower when the inverted STF estimated from the same source is used. To further verify this effect, the same process was repeated by exciting both STFs from Source 16. Misfit values between the synthetic and experimental signals for Source 16 are shown in Fig. 11(b). It is evident from the results presented in Fig. 11(a)–(b) that the inverted STF for a specific source from its own A-scan will provide a more accurate synthetic signal.

## 6.1.4. Influence of receiver number on STF inversion

The source inversion results shown thus far used only A-scan signals. For the receiver elements that are relatively far away from the source, synthetic signals using the estimated STF from A-scan do not match the experimental data as good as the signals from closer receivers. For instance, in Fig. 10(a), the synthetic A-scan signal at Receiver 4 perfectly fits the experimental signal when Source 4 was excited. On the contrary, for the same Source 4, the synthetic signal at Receiver 16 (far from Source 4) has some mismatch with the experimental signal (Fig. 10(b)).

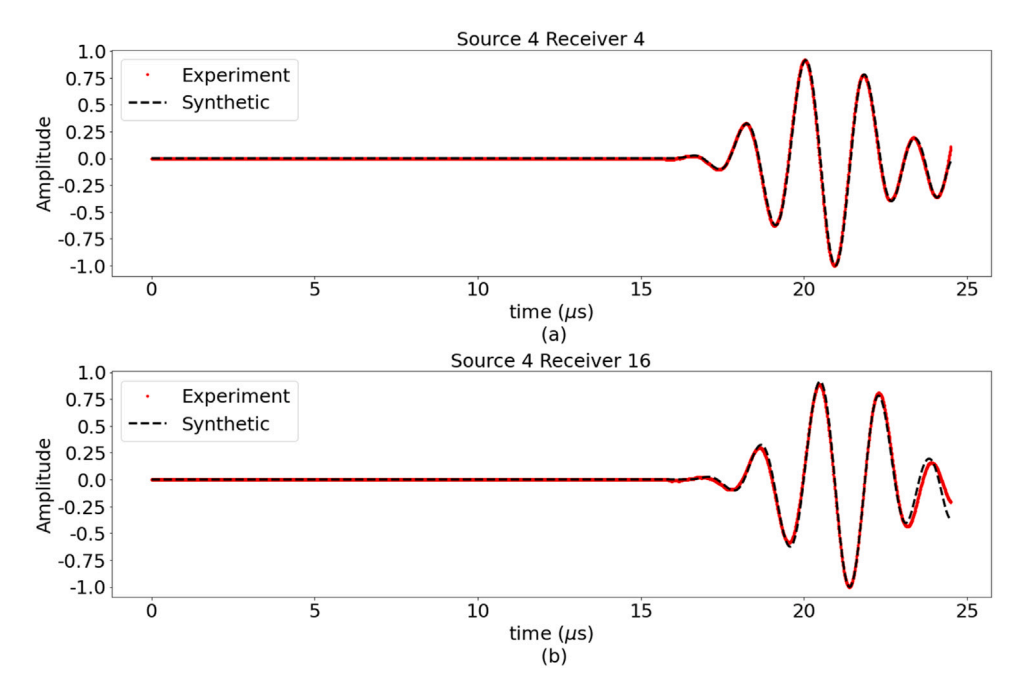


Fig. 10. The comparison of the synthetic and experimental signals at different receiver locations. The synthetic signal exciting the Source 4 of the synthetic model by the estimated STF (shown in Fig. 9(d)) is compared with the experimental signal at (a) Receiver 4, and (b) Receiver 16. The signals at Receiver 4 are closely aligned, whereas there is a small mismatch in Receiver 16 signals.

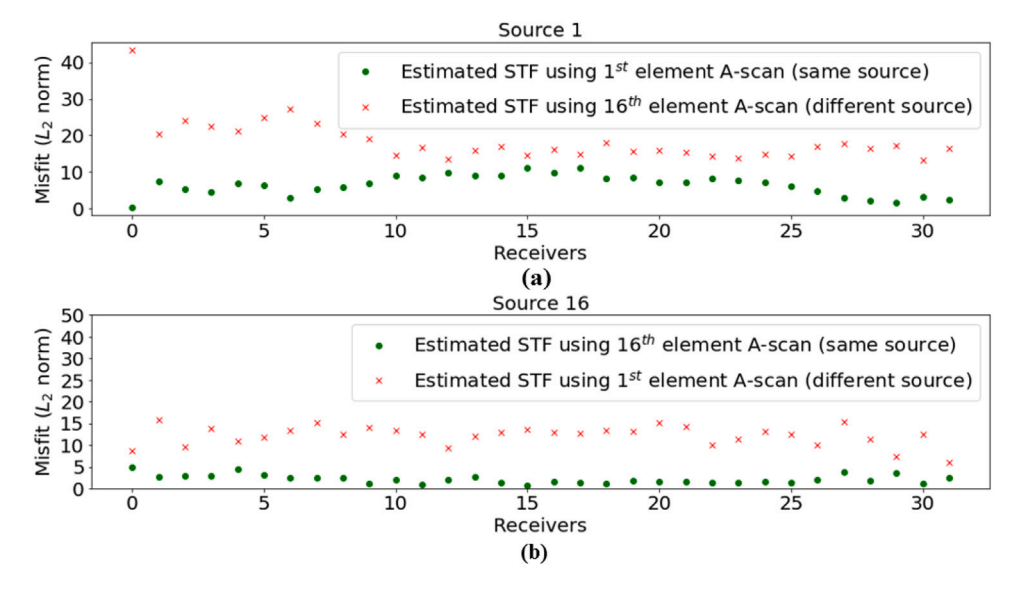


Fig. 11. The  $L_2$  norm misfit between the experimental signals and synthetic signals was evaluated at each receiver location, to illustrate the influence on the synthetic signal if estimated STF for a specific source is employed to a different source. The synthetic signal was acquired using the estimated STF employing A-scan at Receiver 1 and 16, respectively. The computed misfit between the synthetic and experimental signal at each receiver location is compared when excitation is done by (a) Source 1 and (b) Source 16. Red crosses and green dots are the misfit values between synthetic and the experimental signals at each receiver location when the synthetic signals were generated employing the estimated STFs from A-scan signals at Receiver 1 (same source) and Receiver 16 (different source), respectively. The misfit values are lower when the estimated STF for the same source was employed for both Source 1 and Source 16.

To better match the signals from far receivers with experimental measurements, the performance of estimated STFs when signals from multiple receivers were incorporated in source inversion is presented. Two specific cases are compared to highlight this effect: Case 1 – when the source estimation was performed using the A-scan signal at the corresponding receiver location (as described in the previous section) and Case 2 – when the source inversion was performed using signals from the 32 receivers. The same synthetic model as described in Section 4.2 was used for source inversion in both Case 1 and 2.

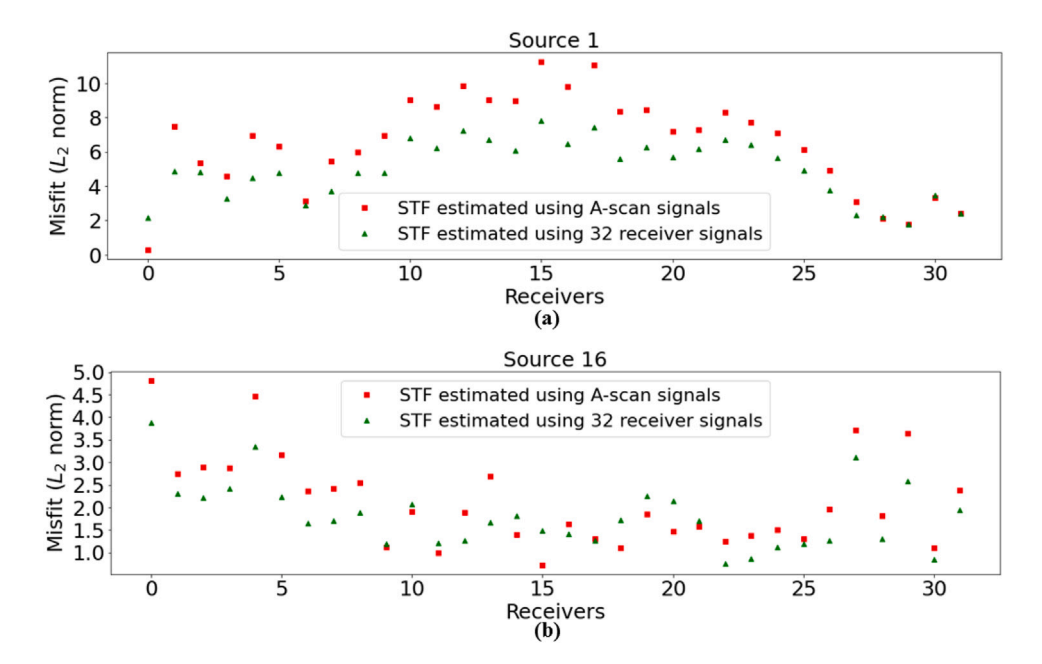


Fig. 12.  $L_2$  norm misfits between the experimental signals and synthetic signals from each acquisition were compared to illustrate the influence of the receiver number on STF inversion when excitation is done by (a) Source 1 and (b) Source 16. Synthetic signals were generated for two specific cases: Case 1 – when the STFs were estimated using the A-scan signal at the corresponding receiver location, and Case 2 – when the STFs were estimated using signals from the 32 receivers. Red squares and green triangles are the misfit values between synthetic and the experimental signals at each receiver location when the synthetic signals were generated considering Case 1 STFs and Case 2 STFs, respectively. The misfit values are lower for most of the receivers that are far away from the source when Case 2 STFs are incorporated to generate synthetic signals. The results verify that the matching accuracy of the signals at receivers far from the source with experimental measurements improves when excitation is done by the STF estimated using 32 received signals.

For Sources 1 and 16, source inversion was performed in Cases 1 and 2, respectively (i.e., a total of four times). Simulations were then performed using the inverted STFs to generate synthetic signals for each case. The  $L_2$ -norm misfits between the synthetic and experimental signals were used to characterize the performance of the STFs in Case 1 and Case 2. The misfit comparison between Case 1 (red squares) and Case 2 (green triangles) is shown in Fig. 12(a) and (b) for Source 1 and Source 16, respectively.

From Fig. 12, it can be observed that the green triangles (Case 2) are below the red squares (Case 1) for most of the receivers that are far away from the source, illustrating that the misfit values are slightly lower using more receivers for STF estimation. For example, when Source 1 was excited by Case 2 STF, as shown in Fig. 12(a), the misfit values are smaller for most of the receivers far from Source 1 (i.e., Receiver 2–28). The misfit values at Receiver 28–32 using Case 2 STF are not lower compared to Case 1 STF as shown in Fig. 12(a). The reason is that the signals from Receiver 28–32 within the considered time window do not contain the tailed region of the P waves, which is the main contributing factor to the misfit values. Similarly, in Fig. 12(b), it is shown that misfit values at far receivers (i.e., Receiver 1–9 and Receiver 22–32) are lower when Source 16 was excited by Case 2 STF. Within the considered time window, the far left and right receivers (i.e., Receivers 1 and 32) contain the full P-wave energy. As a result, for Source 16, synthetic signals at the far most receivers (i.e., Receiver 1 and 32) have lower misfits when excited by Case 2 STF. Therefore, the results presented in Fig. 12 indicate that the far receiver signals align better with the experimental measurements when signals from all receivers are considered in source estimation.

Finally, the synthetic signals generated using the Case 2 STFs are compared with the experimental measurements for all of the signals in Fig. 13. The synthetic signals at each receiver location were very closely aligned with the experimental signals both in the case of Source 1 and Source 16 shown in Fig. 13(a) and (b) respectively, which further verified the accuracy of the Case 2 STFs.

## 6.2. FWI results

In this section, the feasibility of FWI in elastic material characterization using experimentally reconstructed results is evaluated. Initially, the performance of FWI with accurately inverted STFs against wrong STFs is compared. Next, the accuracy of the reconstructed results using a numerical model while employing the estimated STFs in the FWI process is analyzed. Experimental FWI results for a 6061 aluminum specimen are presented, and its potential for material characterization is discussed.

#### 6.2.1. Synthetic reconstruction

To demonstrate the importance of STF accuracy, FWI was performed to study two specific cases: (1) FWI with wrong STFs, and (2) FWI with the inverted STFs. The true model was developed with the longitudinal and shear wave speeds as 6288.7 m/s and 3167.7 m/s, respectively. The wave speeds were analytically computed from the known properties of 6061 aluminum (i.e., Elastic

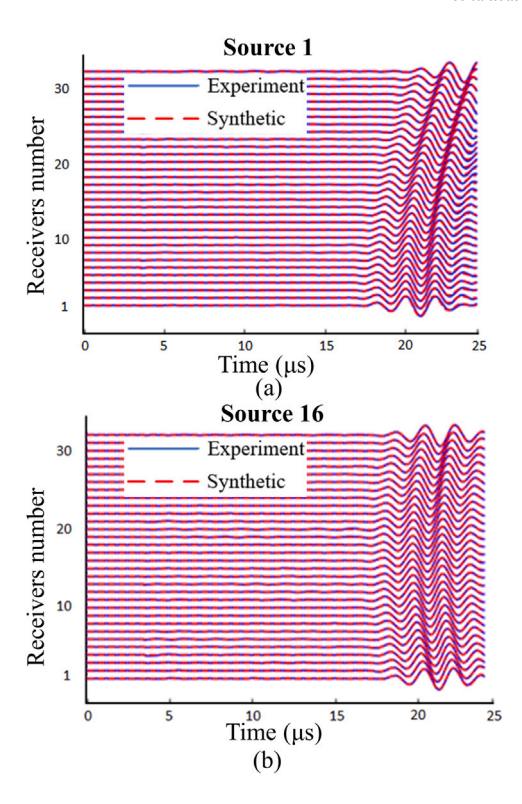


Fig. 13. Received signal comparison between the synthetic and experimental measurements from all the receiver elements for (a) Source 1 and (b) Source 16. STFs in the synthetic model were estimated utilizing all the receivers' signals for Source 1 and Source 16, respectively.

modulus, 70 GPa, and Poisson's ratio, 0.3). The model described in Section 4.2 with  $V_p$  and  $V_s$  of 6410 m/s and 3126.4 m/s was used as the initial model. The longitudinal wave speed distributions of the initial and true model are shown in Fig. 14(a) and (b), respectively.

In the first case, the sources of the true model were excited by a five-peaked tone-burst signal with a center frequency of 0.5 MHz as an unknown STF to generate the observed signals. Then, the reconstruction was done by intentionally exciting the sources with Ricker wavelets with a center frequency of 0.5 MHz to observe the effect of incorrect STFs on the performance of FWI. The inverted  $V_p$  at the 4th iteration is shown in Fig. 14(c). The wave speed distribution in the middle region of the inverted model exceeds 6500 m/s, indicating that the model is not converging towards the true model. Also, significant artifacts are present near the sources/receivers and at the left and right boundaries. As expected, the model parameters fell into a local minimum due to the incorrect STFs in reconstruction.

In the second case, FWI was performed employing STFs that are estimated using signals from 32 receivers (i.e., Case 2 STFs addressed in Section 6.1.4) in the reconstruction to analyze the performance of estimated STFs. The reconstructed  $V_p$  in Fig. 14(d) shows that the middle region of the domain was converging towards the  $V_p$  in the corresponding regions of the true model (–31 mm to 31 mm). In this case study, only one transmitting and one receiver transducer array with an aperture of 62 mm were used to simulate the transmission mode acquisition. Consequently, the model did not update in the side boundary region during the inversion due to limited transducer coverage. The misfit over iterations in case of both incorrect STFs and inverted STFs are shown in Fig. 15(a) and (b), respectively.

From Fig. 15(a), it can be observed that in the case of incorrect STFs, the misfit values over iterations were not converging to a minimum value; instead, the model update stopped at iteration 8. On the contrary, in the case of inverted STFs, the misfit values were reduced over iterations, and after iteration 40, the misfit reduction became slower.

#### 6.2.2. Reconstruction with experimental measurements

The feasibility of FWI in material characterization using experimental data from a 6061 aluminum specimen is considered in this section. To perform FWI, the experimental measurements on the aluminum specimen (shown in Fig. 5) for every possible combination of source-receiver in transmission mode were considered as the observed signals. The same initial model, as discussed in the previous section with  $V_p$  and  $V_s$  of 6410 m/s and 3126.4 m/s, respectively, was used as the starting model. As an example, the wavefield snapshots for Source 15 in the initial model across the elastic medium at 4.9  $\mu$ s, 9.8  $\mu$ s, 14.7  $\mu$ s, and 19.6  $\mu$ s are shown in Fig. 16(a)–(d), respectively. The time-space signals acquired at all 32 receiver positions from Source 15 are presented in Fig. 17, in which only the P-waves are considered in FWI.

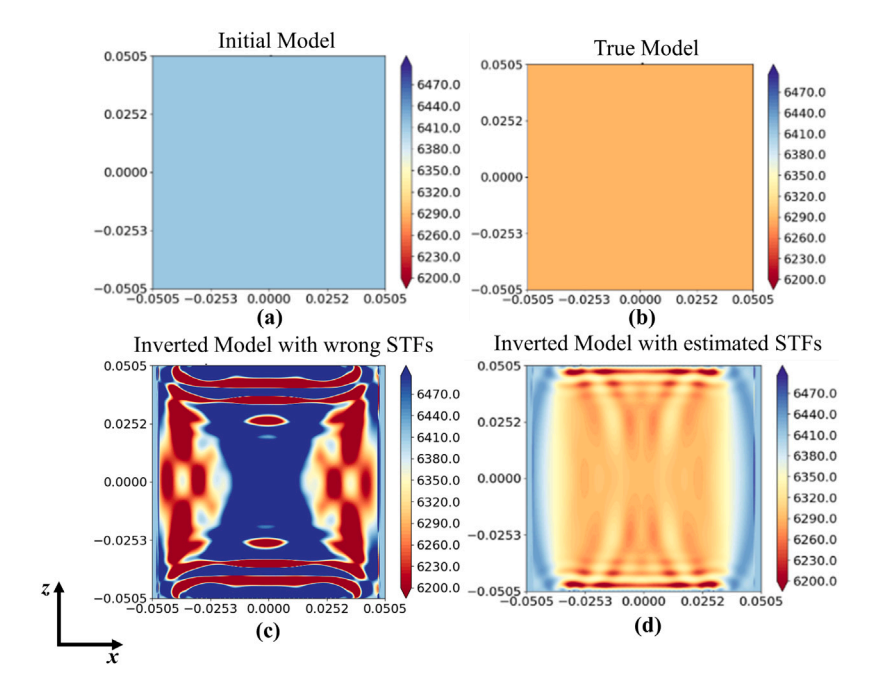


Fig. 14. Longitudinal wave speed distribution of (a) the initial background model, (b) the true model, (c) the inverted model with wrong STFs at iteration 4, and (d) the inverted model using the true model at iteration 19. (In this section, the dimensions of all models are shown in meters.)

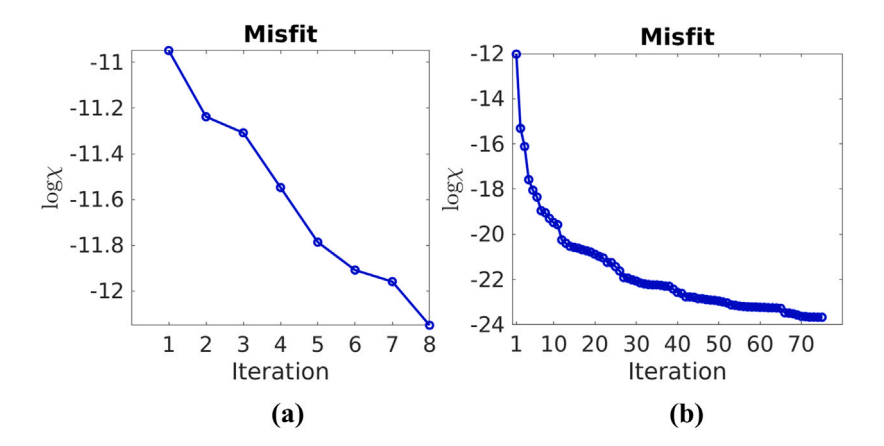


Fig. 15. Data misfit (in log scale) over iteration when inversion was performed with (a) wrong STFs, (b) inverted STFs. In case of wrong STFs, the inversion is not converging and stopped at iteration 8. On the other hand, the misfit values reduced rapidly when inverted STFs were incorporated in the inversion, and after iteration 40, the misfit reduction became slower.

Signals from Source 15 Receiver 20 are presented in Fig. 18 as an example. Fig. 18(a) shows the normalized input STF employed in Source 15 and the experimental measurement from Receiver 20 when Source 15 was excited. The signal changes during the inversion for the Source 15 Receiver 20 are summarized in Fig. 18(b) and (c). The comparison between the normalized signal from the initial model and the experimental measurement is demonstrated in Fig. 18(b), which shows that the initial model's signal differs from the experimental measurement. On the other hand, Fig. 18(c) shows the normalized signal from the inverted model at iteration 11 and the experimental measurement. The signal from the inverted model closely aligns with the experimental measurement, indicating the convergence of the model towards real wave speed (i.e., experimental measurements).

The wave speed distribution of the initial model is shown in Fig. 19(a), and the reconstructed wave speeds at different iterations are shown in Fig. 19(b)–(d). The middle region in the model was updated over each iteration. Fig. 20 shows that data misfits are reducing over iterations, and the misfit reduction diminished after iteration 11. The model started overfitting with the presence of strong artifacts after iteration 11.

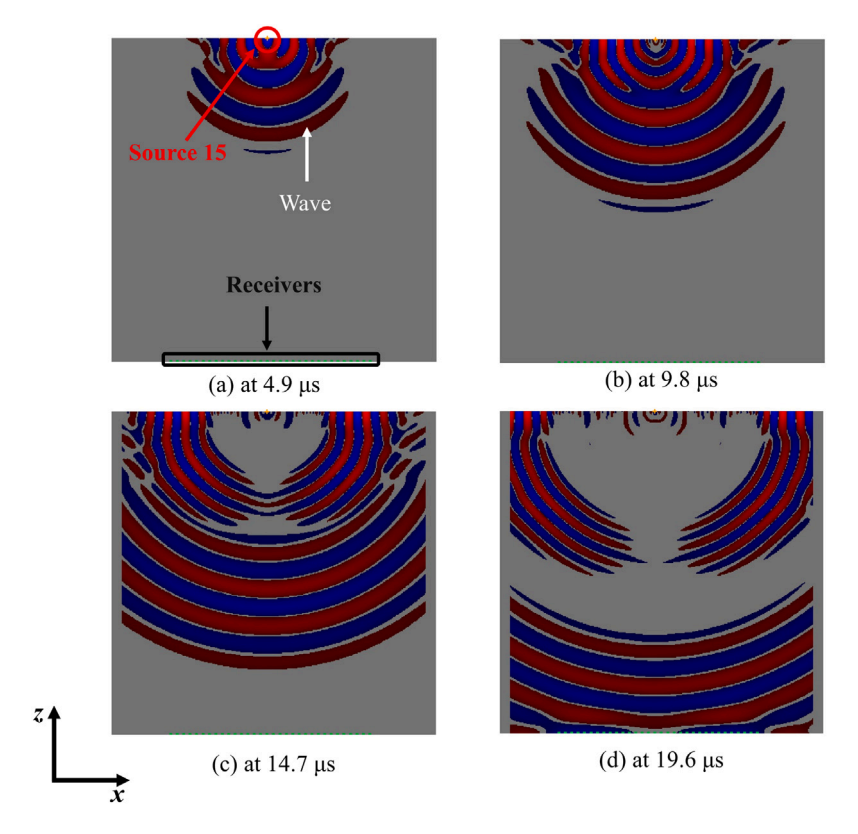


Fig. 16. Wave propagation snapshots (displacement in vertical component) in the initial model for 6061 aluminum specimen at (a) 4.9  $\mu$ s and (b) 9.8  $\mu$ s (c) 14.7  $\mu$ s (d) 19.6  $\mu$ s.

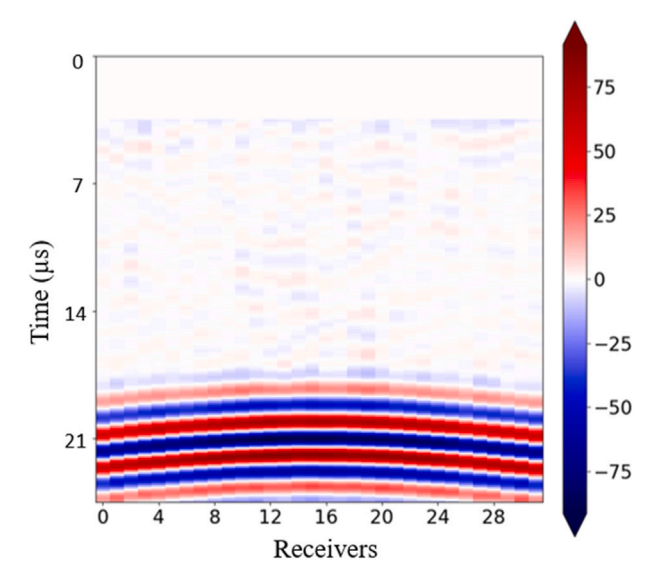


Fig. 17. Time space signal of the experimental measurements for 15th excitation element.

## 6.2.3. Quantitative analysis

To further investigate the inversion results, a line at z = 0 mm across the x - z plane of the synthetic and experimental inverted model was considered (shown in Fig. 21). At z = 0 mm, the velocity distributions of the initial model, true model, synthetic inverted model at the 19th iteration, and experimental inverted model at the 11th iteration are plotted. The center of the domain is assumed to be the reference point. From Fig. 21, it can be observed that for the updated synthetic model,  $V_p$  at the middle (-31 mm to 31 mm)

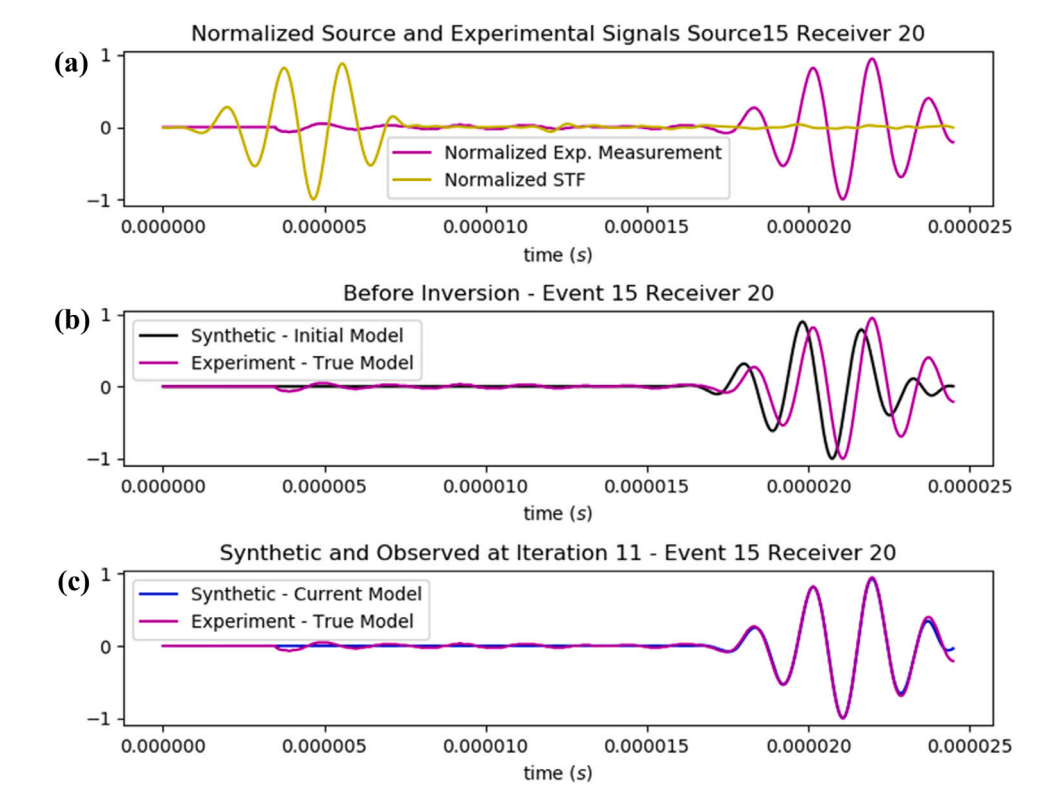


Fig. 18. Individual signals at 'Receiver 20' when Source 15 was excited by the estimated STF. (a) The normalized input STF and the normalized experimental measurement, (b) the synthetic signal with the initial model and the experimental measurement as the true model, and (c) the synthetic signal with the updated model at iteration 11.

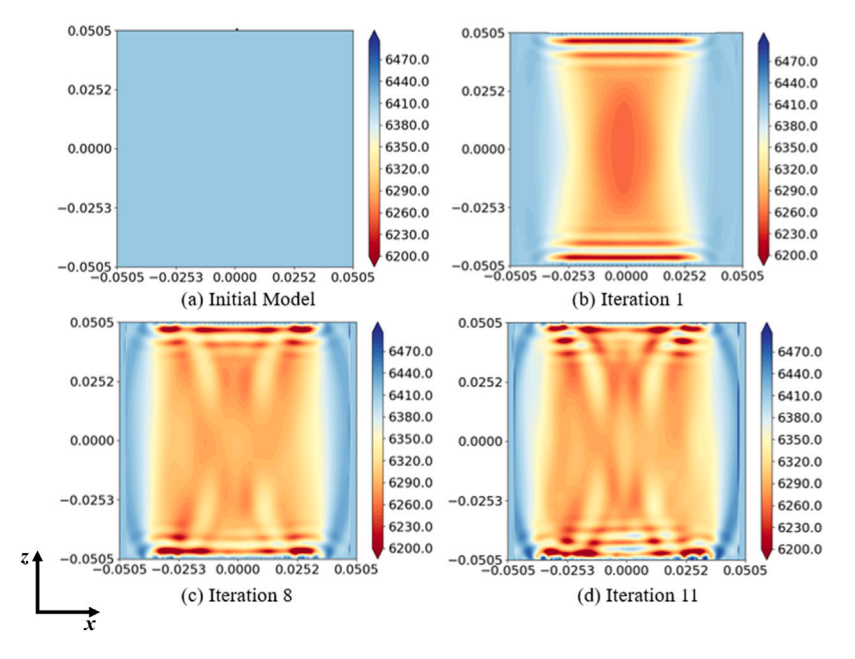


Fig. 19. Inversion results incorporating experimental measurements at different iterations. Experimental signals were acquired from the scanning setup described in Section 4.1. Longitudinal wave speed distribution (a) at the initial model, (b) at iteration 1, (c) at iteration 8, and (d) at iteration 11.

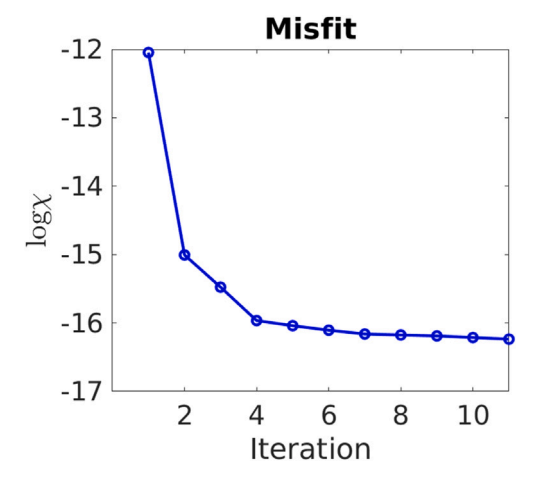


Fig. 20. Data misfit over iterations when the inversion was done using experimental measurement (in log scale).

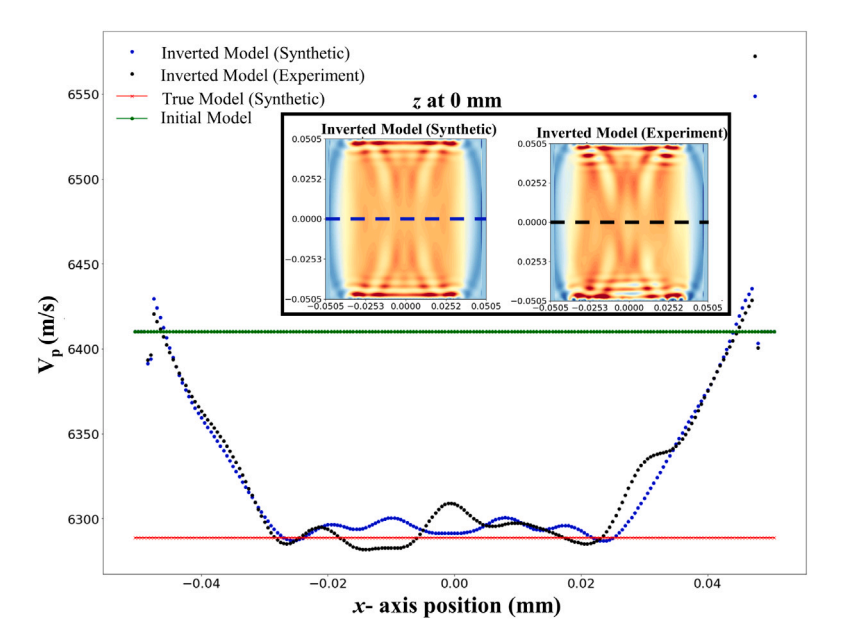


Fig. 21. Longitudinal wave speed distribution along horizontal lines (blue and black dashed lines in the inverted models) at z=0 mm of the synthetic inverted model (blue dots) and inverted model using experimental measurements (black dots). The inverted models are shown in the box. The green and red lines in the figure are the reference wave speed distribution along the horizontal line at z=0 mm for the initial and true models, respectively.

closely converges to the  $V_p$  of the target model at the 11th iteration. For the experimental signal, the variation of the inverted  $V_p$  in the middle (-31 mm to 31 mm) is about 15 m/s, representing about 0.25%, which is comparatively small and further supporting an appreciable FWI performance.

## 6.2.4. Smoothing

In the reconstructed images depicted in Fig. 19, we can observe noticeable artifacts in the form of horizontal strips in close proximity to the sources and receivers, which most likely come from the source-receivers acquisition. Additionally, there are circular artifacts in the middle of the domain due to the wave path effect. The circular artifacts might come from the vertical velocity contrast created by limiting the model laterally. To mitigate these spurious artifacts, a deliberate application of implicit regularization, specifically in the form of smoothing, was employed [75]. In this section, we implemented a 2-D convolution of the unsmoothed gradient kernel with a Gaussian smoothing operator. The Gaussian smoothing operator, applied in the 2-D context, is defined by the Gaussian equation as follows,

$$G(x,y) = \frac{1}{2\pi\sigma^2} e^{-(x^2 + z^2)/2\sigma^2} \quad , \tag{19}$$

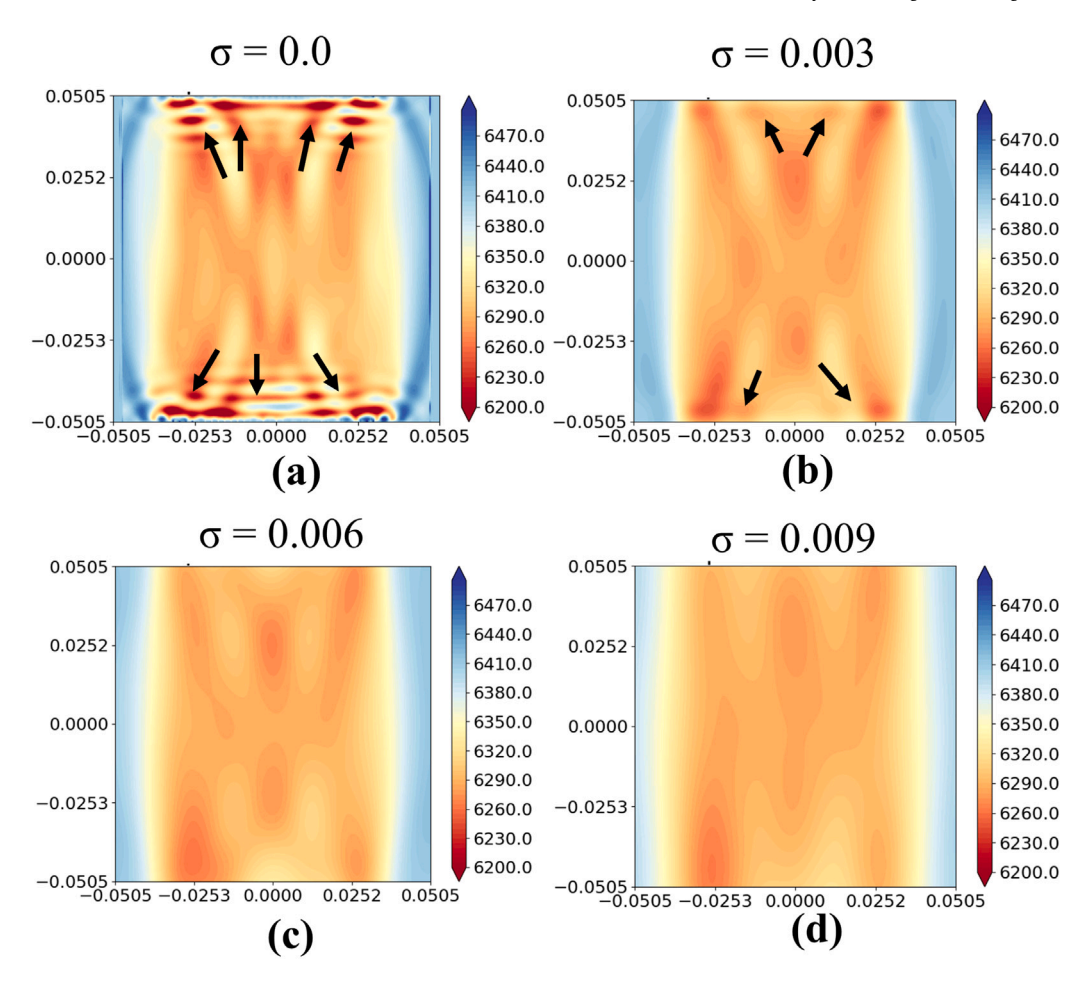


Fig. 22. Experimental reconstruction of longitudinal wave speed  $(V_p)$  model at iteration 11. (a)  $V_p$  model without applying any smoothing ( $\sigma = 0.0$ ). The artifacts due to the sources-receivers acquisitions are pronounced in the vicinity of the sources and receivers (marked by black arrows).  $V_p$  models with Gaussian smoothing, when (b)  $\sigma = 0.003$ , (c)  $\sigma = 0.006$ , and (d)  $\sigma = 0.009$ . Significant artifacts near the sources and receivers are eliminated after applying smoothing. For  $\sigma = 0.003$ , some amount of artifacts still persisted, as marked by the black arrows in (b). Whereas significant artifacts near the sources and receivers are successfully removed for  $\sigma = 0.006$  and  $\sigma = 0.009$ . The artifacts inside the middle of the domain are less pronounced for  $\sigma = 0.009$ .

where x is the distance from the origin in the horizontal axis, z is the distance from the origin in the vertical axis, and  $\sigma$  is the standard deviation of the Gaussian distribution.

To quantitatively assess the smoothing effect, a pivotal step involves the careful selection of the standard deviation, denoted as  $\sigma = \sigma_x = \sigma_z$ . The choice of  $\sigma$  is expressed in terms of grid spacing [75]. Notably, the grid spacing in the model is intricately linked to the dominant wavelength of the excited wave field. Thus, to ensure a reasonable application of smoothing, it is advisable to use scale lengths smaller than the dominant wavelength in the simulation [76]. In our specific model, the dominant frequency was 0.5 MHz (corresponding to a wavelength of approximately 12 mm), and based on that, we selected the smoothing parameter (i.e.,  $\sigma$ ) value closer to the half wavelength.

To verify the effect of smoothing, we performed reconstructions by selecting  $\sigma=0.003,0.006$ , and 0.009. When no smoothing was applied, pronounced artifacts near the sources and receivers were observed, marked by black arrows in Fig. 22a. For  $\sigma=0.003$ , the majority of artifacts near the sources were effectively eliminated, although a small number of artifacts persisted, as depicted by the black arrows in Fig. 22b. Conversely, for  $\sigma=0.006$  and  $\sigma=0.009$ , significant artifacts near the sources and receivers were successfully removed. Notably, for  $\sigma=0.009$ , other artifacts within the domain were less pronounced and the velocity distribution in the middle of the domain (–31 mm to 31 mm) was observed to be uniform (showed in Fig. 23).

## 7. Discussion

Several critical processes, such as selecting the synthetic and experimental time window for each source element, minimizing the system-induced noises in the signal by applying a filter if necessary, and selecting the source frequency in the synthetic model, contributed to the success of this approach. It is also worth mentioning that in case of a poor initial model, some data error might

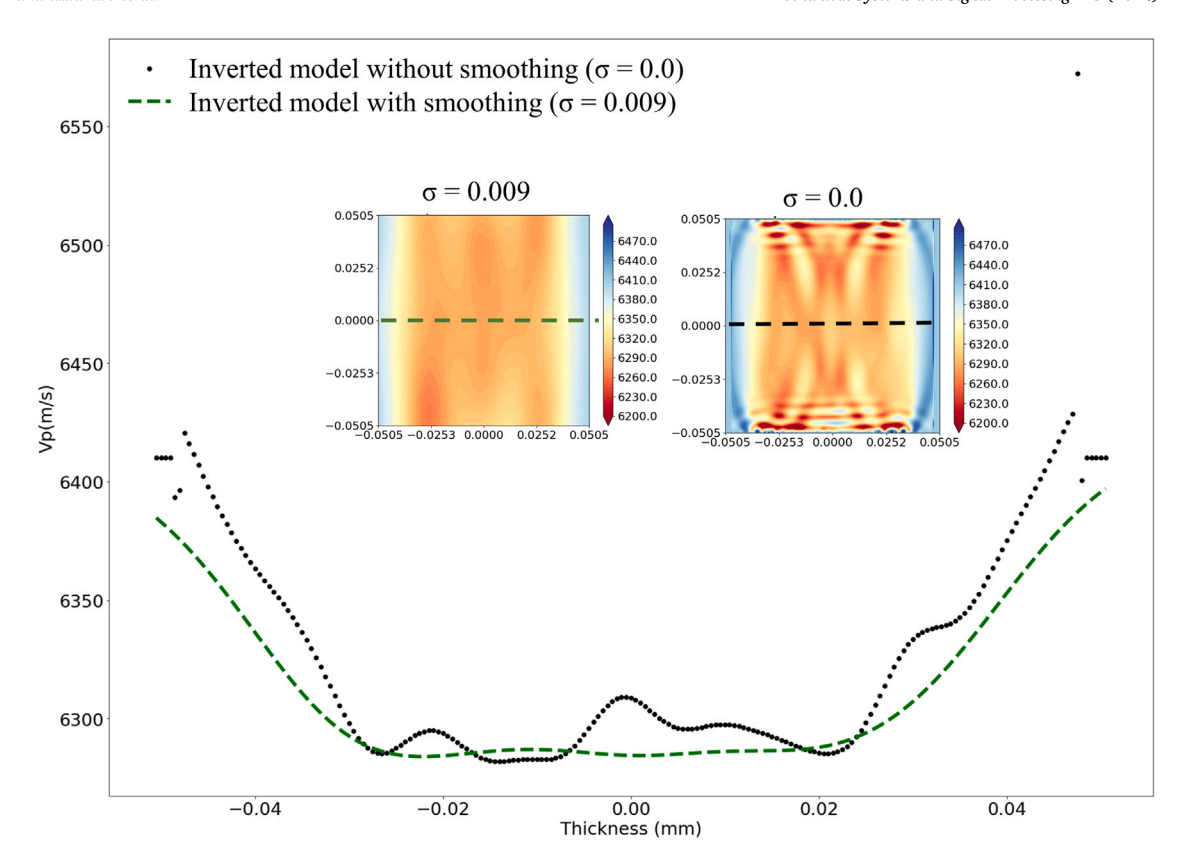


Fig. 23. Longitudinal wave speed distribution along horizontal lines (green and black dashed lines in the inverted models) at z = 0 mm. The black dotted lines are the inverted model without applying Gaussian smoothing ( $\sigma = 0.0$ ), and the green dashed lines in the plot indicate longitudinal wave speed distribution of the inverted model with applying Gaussian smoothing ( $\sigma = 0.009$ ).

manifest in the inverted STFs. In this case, an alternate source and model update might be required. The inverted source wavelet (at each iteration or every so iteration) can also be changed with the model [77].

Another critical step of successful reconstruction is modeling the side boundary reflections, especially when dealing with scanned fine-sized components. The results of an inversion can be affected by reflection from the side borders, particularly for engineering structures with a limited horizontal length. Reflections from the side edges can overlap with scattered signals from internal features in the specimen. In this study, to keep the problem simple, an aluminum sample with a horizontal length three times larger than the vertical length (310 mm) was considered. Therefore, the boundary reflection from the left and right side boundaries cannot affect the signal. As a result, the left and right boundary reflections were neglected, and the perfectly matched layer (PML) [78,79] boundary conditions were introduced in the numerical model. In the future, side boundary reflections will be incorporated into tomographic imaging. Additional information can be captured by allowing waves to reflect off the boundaries, leading to more accurate and higher-quality reconstructed images. However, the implementation of this technique requires a careful modification of the mathematical model and a thorough understanding of the underlying physics of wave propagation.

Several notable aspects of the reconstructed results are also observed. For instance, the model was not updating near the side boundaries both in synthetic reconstructed images (Fig. 14(c)) and reconstructed images using experimental data (Fig. 19). This phenomenon is expected due to the limited coverage of the transducer array. The model domain (101 mm) was larger than the transmitting and receiving transducer's aperture (62 mm), which is placed in the middle of the domain in the transmission mode as shown in Section 4.1. One possible way to resolve this limitation is by implementing a more complex scanning with more sources and receivers surrounding the domain to increase the coverage of the transducer array. However, increasing the number of sources will increase the computational cost. In this current study, the goal is to prove the feasibility of FWI in material characterization. Despite having limited coverage, the proposed model convincingly reconstructed the longitudinal wave speed in the region of interest.

Another limitation is the appearance of the artifacts near the source and receiver locations in the numerical (Fig. 14(c)) and experimental (Fig. 19(d)) reconstructed images. These artifacts may have several causes, such as an inaccurate initial model, potential noise in the data, or errors in numerical discretization [80]. Because of the aforementioned reasons, the higher non-linearity appears in the inverse problem near the acquisition array where the computed gradient is singular. This non-linearity can cause difficulties in accurately reconstructing the image and can lead to artifacts in the final reconstructed image. Freezing the area near the source and receivers during the inversion can significantly lessen these artifacts. Modrak and Tromp [19] provided

several potential solutions, such as using a custom preconditioner or a special filter (i.e., mask) to mute model updates close to the locations of sources and receivers. However, a better adjustment of the approach as well as an improved understanding of the properties of the uninverted zone and source/receiver responses, will probably be needed to limit these problems, and thus require further investigation.

#### 8. Conclusion

This paper proposed an FWI-based ultrasound computed tomography method with an accurate source modeling approach for elastic material characterization. We conclude from the results that the proposed FWI framework shows promise in characterizing different engineering structures with unknown material properties. To benchmark the imaging performance, a numerical model of wave speeds using the spectral element method (SEM) was established. This model represents the isotropic bulk material property variation in microstructures corresponding to varying grain types and sizes, demonstrating the proposed framework's potential in material characterization. One of the main challenges in FWI-based ultrasound tomography is accurate forward modeling, which requires an appropriate definition of the source information. To alleviate this issue, a source modeling approach was introduced that utilizes a linear inverse algorithm to estimate the source time function for modeling the transducer as a mechanical input of a point source in SEM. The working principle of the source inversion process was demonstrated using transmission tomography data from a 6061 aluminum specimen. A systematic performance analysis was presented to validate the accuracy of the estimated STFs. The results show that the simulated signals using the estimated STFs for excitation closely matched with experimental signals such that the accuracy of the estimated STFs was verified. Finally, FWI was implemented on experimental data from a 6061 aluminum specimen with inverted STFs. The results show that the proposed FWI method successfully reconstructed the longitudinal wave speed distribution. With high spatial resolution and sensitivity shown in the transmission scheme using in-house experimental data, FWI with accurate source modeling shows promise to reconstruct the velocity structure within the scanned region effectively. Future works related to this research should focus on improving the reconstruction results by increasing structural complexity and mitigating the artifacts.

## CRediT authorship contribution statement

**Md Aktharuzzaman:** Data curation, Formal analysis, Investigation, Methodology, Validation, Visualization, Writing – original draft, Conceptualization. **Shoaib Anwar:** Investigation, Visualization. **Dmitry Borisov:** Writing – review & editing. **Jiaze He:** Conceptualization, Funding acquisition, Supervision, Writing – review & editing.

#### Declaration of competing interest

The authors declare the following financial interests/personal relationships which may be considered as potential competing interests: Jiaze He reports financial support was provided by NASA. Jiaze He reports financial support was provided by ACCESS.

#### Data availability

Data will be made available on request.

## Acknowledgments

We appreciate the financial support provided by NASA, USA Project #80NSSC22M0223 and the computational resources provided by ACCESS Project #MDE220005.

## References

- [1] A. Vafadar, F. Guzzomi, A. Rassau, K. Hayward, Advances in metal additive manufacturing: a review of common processes, industrial applications, and current challenges, Appl. Sci. 11 (3) (2021) 1213.
- [2] T. Yamazaki, Development of a hybrid multi-tasking machine tool: integration of additive manufacturing technology with CNC machining, Procedia Cirp 42 (2016) 81–86.
- [3] M. Monzón, Z. Ortega, A. Martínez, F. Ortega, Standardization in additive manufacturing: activities carried out by international organizations and projects, Int. J. Adv. Manuf. Technol. 76 (5) (2015) 1111–1121.
- [4] M.K. Thompson, G. Moroni, T. Vaneker, G. Fadel, R.I. Campbell, I. Gibson, A. Bernard, J. Schulz, P. Graf, B. Ahuja, et al., Design for additive manufacturing: Trends, opportunities, considerations, and constraints, CIRP Ann. 65 (2) (2016) 737–760.
- [5] A.M. Beese, Microstructure and mechanical properties of am builds, in: Thermo-Mechanical Modeling of Additive Manufacturing, Elsevier, 2018, pp. 81–92.
- [6] P. Nanekar, B. Shah, Characterization of material properties by ultrasonic, BARC Newslett. 249 (2003).
- [7] D.K. Pandey, S. Pandey, Ultrasonics: A technique of material characterization, Acoust. Waves (2010) 397-430.
- [8] C.H. Gür, B.O. Tuncer, Characterization of microstructural phases of steels by sound velocity measurement, Mater. Charact. 55 (2) (2005) 160-166.
- [9] C.H. Gür, I. Cam, Comparison of magnetic Barkhausen noise and ultrasonic velocity measurements for microstructure evaluation of SAE 1040 and SAE 4140 steels, Mater. Charact. 58 (5) (2007) 447-454.
- [10] I. Mutlu, E. Oktay, S. Ekinci, Characterization of microstructure of H13 tool steel using ultrasonic measurements, Russ. J. Nondestruct. Test. 49 (2) (2013) 112–120.
- [11] M. Schickert, M. Krause, W. Müller, Reconstruction by synthetic aperture focusing technique, Adv. Dev. NDE Tech. Concr. Struct. 15 (3) (2003) 235.

- [12] M. Spies, H. Rieder, A. Dillhöfer, V. Schmitz, W. Müller, Synthetic aperture focusing and time-of-flight diffraction ultrasonic imaging—past and present, J. Nondestruct. Eval. 31 (4) (2012) 310–323.
- [13] K. Hoegh, L. Khazanovich, Extended synthetic aperture focusing technique for ultrasonic imaging of concrete, NDT E Int. 74 (2015) 33-42.
- [14] A. Hormati, I. Jovanović, O. Roy, M. Vetterli, Robust ultrasound travel-time tomography using the bent ray model, in: Medical Imaging 2010: Ultrasonic Imaging, Tomography, and Therapy, Vol. 7629, SPIE, 2010, pp. 165–176.
- [15] R. Stotzka, N.V. Ruiter, T.O. Müller, R. Liu, H. Gemmeke, High resolution image reconstruction in ultrasound computer tomography using deconvolution, in: Medical Imaging 2005: Ultrasonic Imaging and Signal Processing, Vol. 5750, SPIE, 2005, pp. 315–325.
- [16] C. Li, N. Duric, P. Littrup, L. Huang, In vivo breast sound-speed imaging with ultrasound tomography, Ultrasound Med. Biol. 35 (10) (2009) 1615-1628.
- [17] D. Theis, E. Bonomi, Seismic imaging method for medical ultrasound systems, Phys. Rev. A 14 (3) (2020) 034020.
- [18] J. Virieux, S. Operto, An overview of full-waveform inversion in exploration geophysics, Geophysics 74 (6) (2009) WCC1-WCC26.
- [19] R. Modrak, J. Tromp, Seismic waveform inversion best practices: regional, global and exploration test cases, Geophys. J. Int. 206 (3) (2016) 1864-1889.
- [20] R. Huang, Z. Zhang, Z. Wu, Z. Wei, J. Mei, P. Wang, Full-waveform inversion for full-wavefield imaging: Decades in the making, Lead. Edge 40 (5) (2021) 324–334.
- [21] B. Liu, Z. Gong, F. Zhang, X. Xu, Y. Zhao, L. Chen, Full-waveform inversion method for tunnel seismic forward prospecting, Geophys. J. Int. 232 (3) (2023) 2186–2204.
- [22] Y. Lin, J. Theiler, B. Wohlberg, Physics-guided data-driven seismic inversion: Recent progress and future opportunities in full-waveform inversion, IEEE Signal Process. Mag. 40 (1) (2023) 115–133.
- [23] I. Masoni, Inversion of Surface Waves in an Oil and Gas Exploration Context (Ph.D. thesis), Université Grenoble Alpes, 2016.
- [24] O. Hermant, O. Khakimov, C. Barajas, B. Hutahayan, M. Mahgoub, G. Cambois, FWI using reflections in shallow waters offshore Abu Dhabi, in: Abu Dhabi International Petroleum Exhibition and Conference, SPE, 2022, D031S078R002.
- [25] Z. Zhang, Z. Wu, Z. Wei, J. Mei, R. Huang, P. Wang, Enhancing salt model resolution and subsalt imaging with elastic FWI, Lead. Edge 42 (3) (2023) 207–215.
- [26] S.M. Hanasoge, J. Tromp, Full waveform inversion for time-distance helioseismology, Astrophys. J. 784 (1) (2014) 69.
- [27] S.M. Hanasoge, Full waveform inversion of solar interior flows, Astrophys. J. 797 (1) (2014) 23.
- [28] L. Guasch, O. Calderón Agudo, M.-X. Tang, P. Nachev, M. Warner, Full-waveform inversion imaging of the human brain, NPJ Digit. Med. 3 (1) (2020) 28.
- [29] T.D. Nguyen, K.T. Tran, N. Gucunski, Detection of bridge-deck delamination using full ultrasonic waveform tomography, J. Infrastruct. Syst. 23 (2) (2017) 04016027.
- [30] D. Köhn, T. Meier, M. Fehr, D. De Nil, M. Auras, Application of 2D elastic Rayleigh waveform inversion to ultrasonic laboratory and field data, Near Surf. Geophys. 14 (5) (2016) 461–467.
- [31] J. Rao, M. Ratassepp, Z. Fan, Guided wave tomography based on full waveform inversion, IEEE Trans. Ultrason. Ferroelectr. Freq. Control 63 (5) (2016) 737–745.
- [32] J. Rao, M. Ratassepp, Z. Fan, Limited-view ultrasonic guided wave tomography using an adaptive regularization method, J. Appl. Phys. 120 (19) (2016) 194902.
- [33] J. Rao, M. Ratassepp, Z. Fan, Investigation of the reconstruction accuracy of guided wave tomography using full waveform inversion, J. Sound Vib. 400 (2017) 317-328.
- [34] J. He, J. Rao, J.D. Fleming, H.N. Gharti, L.T. Nguyen, G. Morrison, Numerical ultrasonic full waveform inversion (FWI) for complex structures in coupled 2D solid/fluid media, Smart Mater. Struct. 30 (8) (2021) 085044.
- [35] S. Anwar, J. He, M. Aktharuzzaman, B. Rupp, Numerical studies on inclusion and porosity imaging for additive manufacturing using full waveform inversion, 2022.
- [36] S. Anwar, M. Aktharuzzaman, J. Day, J. He, Ultrasonic multi-hole imaging using full waveform inversion, in: Structural Health Monitoring 2023, 2023.
- [37] J. Tromp, C. Tape, Q. Liu, Seismic tomography, adjoint methods, time reversal and banana-doughnut kernels, Geophys. J. Int. 160 (1) (2005) 195-216.
- [38] R.-E. Plessix, A review of the adjoint-state method for computing the gradient of a functional with geophysical applications, Geophys. J. Int. 167 (2) (2006) 495–503.
- [39] M. Warner, A. Ratcliffe, T. Nangoo, J. Morgan, A. Umpleby, N. Shah, V. Vinje, I. Štekl, L. Guasch, C. Win, et al., Anisotropic 3D full-waveform inversion, Geophysics 78 (2) (2013) R59–R80.
- [40] L. Skopintseva, F. Maaø, Ø. Pedersen, Importance of the source estimation in FWI-sensitivity and examples, in: 78th EAGE Conference and Exhibition 2016, Vol. 2016, EAGE Publications BV, 2016, pp. 1–5.
- [41] N.N. Abboud, G.L. Wojcik, D.K. Vaughan, J. Mould Jr., D.J. Powell, L. Nikodym, Finite element modeling for ultrasonic transducers, in: Medical Imaging 1998: Ultrasonic Transducer Engineering, Vol. 3341, SPIE, 1998, pp. 19–42.
- [42] M. Masouleh, F. Honarvar, Finite element modeling of ultrasonic transducers, in: 4th Iranian International NDT Conference, 2017.
- [43] Z.-P. Chi, Z.-P. Zhao, N. Li, The modeling of piezoelectric transducers using the FDTD method, in: 2008 International Conference on Machine Learning and Cybernetics, Vol. 4, IEEE, 2008, pp. 2154–2159.
- [44] D. Andrews, Modelling of ultrasonic transducers and ultrasonic wave propagation for commercial applications using finite elements with experimental visualization of waves for validation, in: Proceedings of the 2014 COMSOL Conference in Cambridge, Churchill College/University of Cambridge Cambridge, UK 2014
- [45] J. Xu, R. Huanhuan, Design and finite element simulation of an ultrasonic transducer of two piezoelectric discs, J. Meas. Eng. 5 (4) (2017) 266-272.
- [46] R.G. Pratt, Seismic waveform inversion in the frequency domain, part 1: Theory and verification in a physical scale model, Geophysics 64 (3) (1999) 888-901
- [47] G. Sandhu, C. Li, O. Roy, S. Schmidt, N. Duric, Frequency domain ultrasound waveform tomography: breast imaging using a ring transducer, Phys. Med. Biol. 60 (14) (2015) 5381.
- [48] A. Suzuki, Y. Tsubota, T. Terada, H. Yamashita, F. Kato, M. Nishida, M. Satoh, K.-i. Kawabata, Optimized source estimation for full waveform inversion in ultrasound computed tomography, in: Medical Imaging 2021: Ultrasonic Imaging and Tomography, Vol. 11602, SPIE, 2021, pp. 32–39.
- [49] M. Aktharuzzaman, S. Anwar, D. Borisov, J. Rao, J. He, 2D numerical ultrasound computed tomography for elastic material properties in metals, in: ASME International Mechanical Engineering Congress and Exposition, Vol. 86625, American Society of Mechanical Engineers, 2022, V001T01A012.
- [50] J. Tromp, D. Komatitsch, Q. Liu, Spectral-element and adjoint methods in seismology, Commun. Comput. Phys. 3 (1) (2008) 1-32.
- [51] M. Chen, J. Tromp, Theoretical and numerical investigations of global and regional seismic wave propagation in weakly anisotropic earth models, Geophys. J. Int. 168 (3) (2007) 1130–1152.
- [52] A. Tarantola, Inversion of seismic reflection data in the acoustic approximation, Geophysics 49 (8) (1984) 1259-1266.
- [53] J. He, D. Borisov, J.D. Fleming, M. Kasemer, Subsurface polycrystalline reconstruction based on full waveform inversion-a 2D numerical study, Materialia 24 (2022) 101482.
- [54] E. Bozdağ, J. Trampert, J. Tromp, Misfit functions for full waveform inversion based on instantaneous phase and envelope measurements, Geophys. J. Int. 185 (2) (2011) 845–870.
- [55] Y. Luo, Seismic Imaging and Inversion Based on Spectral-Element and Adjoint Methods (Ph.D. thesis), Princeton University, 2012.
- [56] J. Nocedal, S. Wright, Numerical Optimization, 2nd ed., Springer, New York, 2006.

- [57] A. Keramat, H.-F. Duan, B. Pan, Q. Hou, Gradient-based optimization for spectral-based multiple-leak identification, Mech. Syst. Signal Process. 171 (2022) 108840
- [58] M.S. Daoud, M. Shehab, H.M. Al-Mimi, L. Abualigah, R.A. Zitar, M.K.Y. Shambour, Gradient-based optimizer (GBO): A review, theory, variants, and applications. Arch. Comput. Methods Eng. (2022) 1–19.
- [59] E. Biondi, B. Biondi, G. Barnier, Understanding the difference between full Newton and Gauss-Newton approximation of the full waveform inversion Hessian: a short note.
- [60] S. Wright, J. Nocedal, et al., Numerical optimization, Springer Sci. 35 (67-68) (1999) 7.
- [61] W. Zhang, Y. Li, Elastic wave full-waveform inversion in the time domain by the trust region method, J. Appl. Geophys. 197 (2022) 104540.
- [62] J. Nocedal, Updating quasi-Newton matrices with limited storage, Math. Comput. 35 (151) (1980) 773-782.
- [63] S.A. Abdul Karim, M. Iqbal, A. Shafie, M. Izzatullah, Gauss-Newton and L-BFGS methods in full waveform inversion (FWI), in: Proceedings of the 6th International Conference on Fundamental and Applied Sciences: ICFAS 2020, Springer, 2022, pp. 705–713.
- [64] M. Norouzian, S. Islam, J.A. Turner, Influence of microstructural grain-size distribution on ultrasonic scattering, Ultrasonics 102 (2020) 106032.
- [65] L.D. Sotelo, H. Hadidi, C.S. Pratt, M.P. Sealy, J.A. Turner, Ultrasonic mapping of hybrid additively manufactured 420 stainless steel, Ultrasonics 110 (2021) 106269.
- [66] A. Moreau, S.E. Kruger, M. Côté, P. Bocher, In-situ monitoring of microstructure during thermomechanical simulations using laser-ultrasonics, in: 1st International Symposium on Laser Ultrasonics: Science, Technology and Applications, 2008.
- [67] O. Rivera, P. Allison, J. Jordon, O. Rodriguez, L. Brewer, Z. McClelland, W. Whittington, D. Francis, J. Su, R. Martens, et al., Microstructures and mechanical behavior of inconel 625 fabricated by solid-state additive manufacturing, Mater. Sci. Eng. A 694 (2017) 1–9.
- [68] R.T. Modrak, D. Borisov, M. Lefebvre, J. Tromp, SeisFlows—Flexible waveform inversion software, Comput. Geosci. 115 (2018) 88-95.
- [69] P. Dryburgh, R.J. Smith, P. Marrow, S.J. Lainé, S.D. Sharples, M. Clark, W. Li, Determining the crystallographic orientation of hexagonal crystal structure materials with surface acoustic wave velocity measurements, Ultrasonics 108 (2020) 106171.
- [70] T. Thréard, E. de Lima Savi, S. Avanesyan, N. Chigarev, Z. Hua, V. Tournat, V.E. Gusev, D.H. Hurley, S. Raetz, Photoacoustic 3-D imaging of polycrystalline microstructure improved with transverse acoustic waves, Photoacoustics 23 (2021) 100286.
- [71] S.J. Patey, J.P. Corcoran, Physics of ultrasound, Anaesth. Intensive Care Med. 22 (1) (2021) 58-63.
- [72] J. Wiskin, D. Borup, E. Iuanow, J. Klock, M.W. Lenox, 3-d nonlinear acoustic inverse scattering: Algorithm and quantitative results, IEEE Trans. Ultrason. Ferroelectr. Freq. Control 64 (8) (2017) 1161–1174.
- [73] K.J. Marfurt, Seismic modeling: a frequency-domain/finite-element approach, in: SEG Technical Program Expanded Abstracts 1984, Society of Exploration Geophysicists, 1984, pp. 633–634.
- [74] Z.-M. Song, P.R. Williamson, Frequency-domain acoustic-wave modeling and inversion of crosshole data: Part I—2.5-D modeling method, Geophysics 60 (3) (1995) 784–795.
- [75] O. Liu, Y. Gu, Seismic imaging: From classical to adjoint tomography, Tectonophysics 566 (2012) 31-66.
- [76] C. Tape, Q. Liu, J. Tromp, Finite-frequency tomography using adjoint methods—Methodology and examples using membrane surface waves, Geophys. J. Int. 168 (3) (2007) 1105–1129.
- [77] D. Borisov, F. Gao, P. Williamson, J. Tromp, Application of 2D full-waveform inversion on exploration land dataapplication of 2D FWI on land data, Geophysics 85 (2) (2020) R75–R86.
- [78] J.-P. Berenger, A perfectly matched layer for the absorption of electromagnetic waves, J. Comput. Phys. 114 (2) (1994) 185-200.
- [79] W.C. Chew, Q. Liu, Perfectly matched layers for elastodynamics: a new absorbing boundary condition, J. Comput. Acoust. 4 (04) (1996) 341-359.
- [80] F. Bretaudeau, R. Brossier, D. Leparoux, O. Abraham, J. Virieux, 2D elastic full-waveform imaging of the near-surface: application to synthetic and physical modelling data sets, Near Surf. Geophys. 11 (3) (2013) 307–316.